Nano Research

ISSN 1998-0124 CN 11-5974/O4
https://doi.org/10.26599/NR.2026.94909254

Research Article

Flexible pyramidal $BiFeO_3$–$BaTiO_3$ microcone arrays integrated with P(VDF-TrFE) for self-powered mechanical sensing and energy harvesting

Wentao Yang[1,§], Hang Zhan[1,§], Panpan Lv[1](✉), Guiyun Gao[1], Shuzhi Zhang[1], Le Xin[2], Cuncheng Li[1], Luchao Ren[1], Jin Qian[3](✉), Mingwei Zhang[1,4,5](✉)

[1] Discipline and Technology Center for High Temperature Functional Ceramics, Shandong Key Laboratory of Functional-Structural Integrated Ceramics, School of Materials Science and Engineering, Shandong University of Technology, Zibo 255000, China

[2] Department of Mathematics and Physics, Zibo Normal College, Zibo 255130, China

[3] Functional Materials Research Laboratory, School of Materials Science and Engineering, Tongji University, Shanghai 201804, China

[4] Analytical Testing Center, Shandong University of Technology, Zibo 255000, China

[5] Hubei Key Laboratory of Micro-Nanoelectronic Materials and Devices, Hubei University, Hubei 430062, China

[§] Wentao Yang and Hang Zhan contributed equally to this work.

Nano Res., **Just Accepted Manuscript** • https://doi.org/10.26599/NR.2026.94909254

https://www.sciopen.com/journal/1998-0124 on Oct. 12, 2026

© The Authors(s)

Just Accepted

This is a "Just Accepted" manuscript, which has been examined by the peer-review process and has been accepted for publication. A "Just Accepted" manuscript is published online shortly after its acceptance,which is prior to technical editing and formatting and author proofing. Tsinghua University Press (TUP) provides "Just Accepted" as an optional and free service which allows authors to make their results available to the research community as soon as possible after acceptance. After a manuscript has been technically edited and formatted, and the page proofs have been corrected, it will be removed from the "Just Accepted" web site and published officially with volume and article number (e.g., *Nano Research*, **2025**, *18*, 94906990). Please note that technical editing may introduce minor changes to the manuscript text and/or graphics which may affect the content, and all legal disclaimers that apply to the journal pertain. In no event shall TUP be held responsible for errors or consequences arising from the use of any information contained in these "Just Accepted" manuscripts. To cite this anuscript please use its Digital Object Identifier (DOI®),which is identical for all formats of publication.

Flexible pyramidal $BiFeO_3$–$BaTiO_3$ microcone arrays integrated with P(VDF-TrFE) for self-powered mechanical sensing and energy harvesting

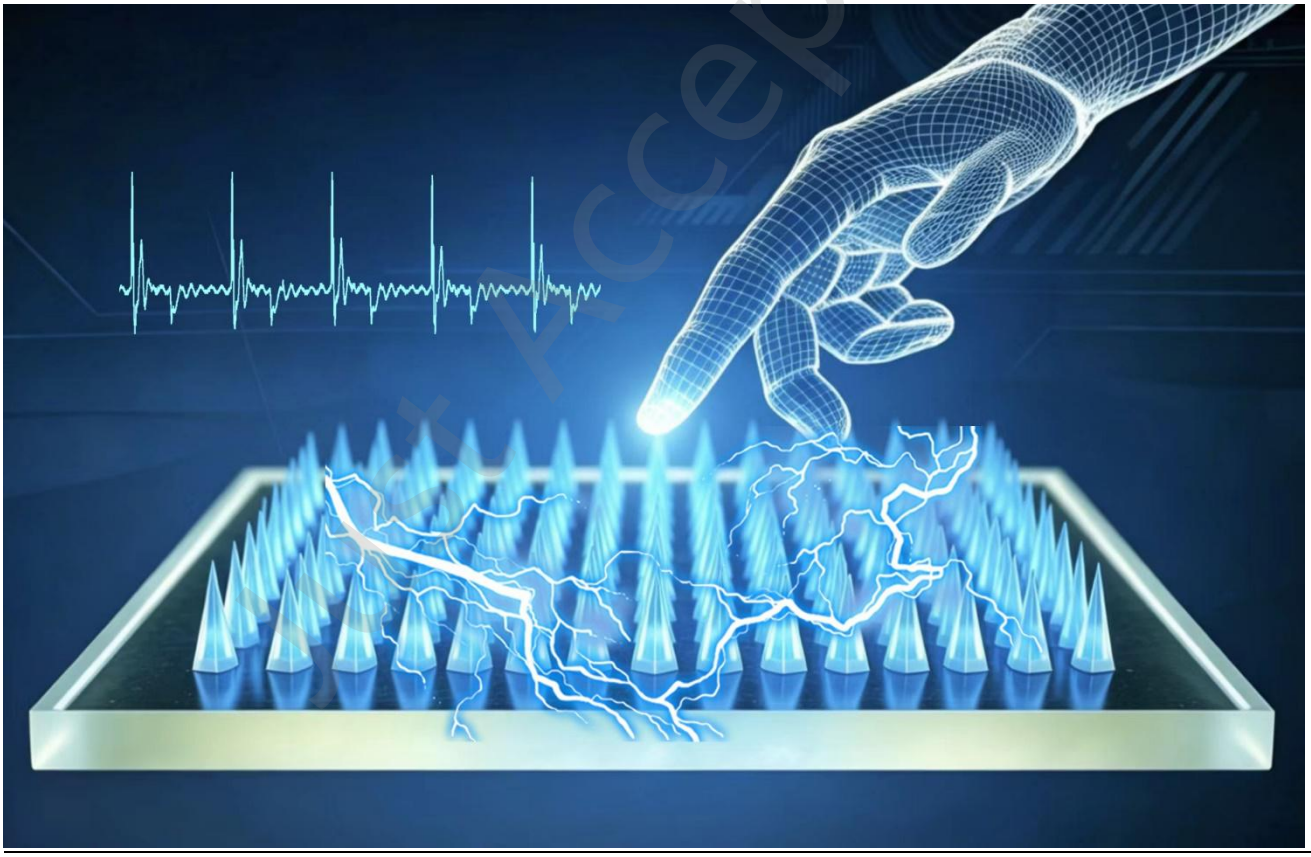
Wentao Yang[1,†], Hang Zhan[1,†], Panpan Lv[1] ✉, Guiyun Gao[1], Shuzhi Zhang[1], Le Xin[2], Cuncheng Li[1], Luchao Ren[1], Jin Qian[3] ✉, Mingwei Zhang[1,4,5,] ✉

[1] *Discipline and Technology Center for High Temperature Functional Ceramics, Shandong Key Laboratory of Functional-Structural Integrated Ceramics, School of Materials Science and Engineering, Shandong University of Technology, Zibo 255000, China*
[2] *Department of Mathematics and Physics, Zibo Normal College, Zibo 255130, China*
[3] *Functional Materials Research Laboratory, School of Materials Science and Engineering, Tongji University, Shanghai 201804, China*
[4] *Analytical Testing Center, Shandong University of Technology, Zibo 255000, China*
[5] *Hubei Key Laboratory of Micro-Nanoelectronic Materials and Devices, Hubei University, Hubei 430062, China*
† The authors contribute equally.

©The Authors(s)

Just Accepted

TABLE OF CONTENTS (TOC)



Vertically oriented $BiFeO_3$-$BaTiO_3$ microcone arrays are constructed in P(VDF-TrFE) films to induce interfacial stress concentration and enhance piezoelectric output. The resulting flexible piezoelectric sensors enable highly sensitive and durable monitoring of human physiological and mechanical motions.

Nano Research

Open Access

Research Article

Flexible pyramidal $BiFeO_3$–$BaTiO_3$ microcone arrays integrated with P(VDF-TrFE) for self-powered mechanical sensing and energy harvesting

Wentao Yang[1,§], Hang Zhan[1,§], Panpan Lv[1] ✉, Guiyun Gao[1], Shuzhi Zhang[1], Le Xin[2], Cuncheng Li[1], Luchao Ren[1], Jin Qian[3] ✉, and Mingwei Zhang[1,4,5] ✉

[1] *Discipline and Technology Center for High Temperature Functional Ceramics, Shandong Key Laboratory of Functional-Structural Integrated Ceramics, School of Materials Science and Engineering, Shandong University of Technology, Zibo 255000, China*
[2] *Department of Mathematics and Physics, Zibo Normal College, Zibo 255130, China*
[3] *Functional Materials Research Laboratory, School of Materials Science and Engineering, Tongji University, Shanghai 201804, China*
[4] *Analytical Testing Center, Shandong University of Technology, Zibo 255000, China*
[5] *Hubei Key Laboratory of Micro-Nanoelectronic Materials and Devices, Hubei University, Hubei 430062, China*
§ *Wentao Yang and Hang Zhan contributed equally to this work.*

Received: 8 August 2026; **Revised:** 29 September 2026; **Accepted:** 12 October 2026

✉ Address correspondence to Panpan Lv, lvpp@sdut.edu.cn; Jin Qian, j28_qian@163.com; Mingwei Zhang, zhang6666666@163.com

Cite this article: *Nano Research*, 2026, 19, 94909254 https://doi.org/10.26599/NR.2026.94909254

ABSTRACT: Flexible piezoelectric composites hold great promise for self-powered sensors and wearable electronics, but their performance is often limited by the low piezoelectricity of polymers, uneven dispersion of inorganic fillers, and poor interfacial stress transfer. To overcome these challenges, we fabricated a vertically oriented pyramidal $BiFeO_3$-$BaTiO_3$ (BFO-BTO) microcone array on P(VDF-TrFE) films using an AAO template-assisted method. The conical geometry induces localized stress concentration at the interface, thereby amplifying the local strain and enhancing the electromechanical response. Systematic studies reveal that microcone height critically influences the polarization behavior, piezoelectric coefficients, and overall device output. The resulting flexible devices, fabricated from the 1.5 μm BFO-BTO microcone/P(VDF-TrFE) composite piezoelectric films, achieve an open-circuit voltage of 5.12 V, a force sensitivity of 6.28 $V \cdot N^{-1}$ (linearity R^2 = 0.98), while maintaining stable performance over 3000 mechanical cycles at 5 Hz under 0.66 N, demonstrating excellent durability. Moreover, the sensors enable high-precision, real-time monitoring of physiological and motion signals, including finger tapping, fist impacts, and foot stepping, highlighting their potential in intelligent health monitoring, human-machine interaction, and mechanical energy harvesting. This work elucidates how microcone structure design governs the electromechanical properties of flexible piezoelectric composites and offers practical design guidelines for flexible sensing and energy-harvesting applications.
KEYWORDS: flexible, piezoelectric composites, microcone arrays, energy harvesting

Just Accepted

INTRODUCTION

Against the backdrop of the accelerating depletion of fossil fuel resources and the continuous increase in carbon emissions, it has become increasingly recognized that the development of renewable clean energy sources, such as wind, solar, and tidal energy, is of great significance for replacing traditional fossil fuels and promoting the advancement of clean and sustainable energy technologies, which is essential for supporting the development of future smart societies.[1-3] Although renewable energy sources are abundant, their large-scale utilization remains limited by various practical constraints.[4,5] In contrast, ubiquitous low-frequency mechanical energy in the environment, such as human motion and daily vibrations, provides another highly promising pathway for energy harvesting.[6-8] Meanwhile, the rapid development of flexible wearable electronic devices in fields such as health monitoring, human-machine interaction, and artificial intelligence has created an urgent demand for lightweight, flexible, and self-powered sensing and energy-supply units.[9-17] Driven by these dual trends, piezoelectric materials, with their ability to directly convert environmental mechanical energy into electrical energy, have demonstrated unique advantages.[18-22] Such weak yet continuous mechanical excitations can be directly converted into electrical energy without an external power source. Moreover, the simple device architecture facilitates miniaturization and flexible integration, making piezoelectric devices particularly suitable for emerging applications such as wearable electronics, self-powered sensing, and Internet of Things (IoT) terminals.[18,23]

Among various piezoelectric materials, inorganic piezoelectric ceramics such as lead zirconate titanate ($Pb(Zr,Ti)O_3$, PZT),[24,25] barium titanate ($BaTiO_3$, BTO),[26,27] and bismuth ferrite ($BiFeO_3$, BFO)[28,29] exhibit excellent intrinsic piezoelectric properties. However, the toxicity of lead in PZT has raised increasing environmental and health concerns, motivating the development of lead-free alternatives such as BFO- or BTO-based systems.[30,31] Nevertheless, the inherent rigidity

and brittleness of these inorganic ceramics limit their direct application in flexible wearable devices.[32] In contrast, organic piezoelectric materials, primarily polyvinylidene fluoride (PVDF) and its copolymer P(VDF-TrFE), offer excellent mechanical flexibility, easy processability, and good biocompatibility,[33,34] making them ideal candidates for large-area tactile sensors and energy harvesting from human activities.[35] Nevertheless, their relatively low intrinsic piezoelectricity results in piezoelectric devices based on these polymers producing significantly lower output power compared with conventional inorganic materials, making it challenging to meet the energy demands of self-powered electronic devices.[23,36] Consequently, the development of high-performance organic-inorganic composite materials has become a major research focus.[37,38] In particular, inorganic fillers are often incorporated into organic matrices to develop flexible composite materials that can combine the superior piezoelectric properties of inorganic components with the mechanical flexibility of polymers, making them suitable for wearable devices.[39] Among various composite materials, PVDF-based composites with functional fillers have been widely explored for piezoelectric sensing and energy harvesting, showing enhanced electrical output performance.[40-42] PVDF not only serves as a structural support but also contributes to the piezoelectric output of the composite materials.[43] Piezoelectric fillers act as nucleating agents to promote PVDF crystallization while providing additional piezoelectric effects.[38] For example, Tian *et al.* added PZT particles to the PVDF matrix to prepare composite piezoelectric films.[44] However, random filler dispersion in the polymer matrix presents several challenges: fillers tend to aggregate in the polymer matrix, leading to an increase in interface defects and local stress concentration, which may even cause composite film fracture.[45] In addition, aggregation reduces the ability of the fillers to induce polymer crystallization, making it difficult to significantly enhance the content of the piezoelectric β phase.[46]

Beyond material modification, structural optimization serves as a complementary approach. As demonstrated in previous studies, flat thin films exhibit limited deformation capacity under out-of-plane compression, which often restricts key performance metrics such as sensitivity and effective detection range. In contrast, the introduction of micro/nanostructures can enhance mechanical deformability by exploiting structural size effects. For example, Chen *et al.* demonstrated that introducing a mesoporous architecture into PVDF films could enhance compressibility and electromechanical coupling, leading to a 100% increase in piezoelectric output compared with dense solid films.[47] Similarly, Lee *et al.* showed that micropatterning P(VDF-TrFE) films into trigonal-line or pyramid geometries markedly increased deformation under vertical compression, yielding nearly fivefold higher piezoelectric output than that of flat films.[48] More recently, Yin *et al.* showed that hierarchical microstructures can improve piezoelectric sensing performance by enhancing stress concentration and mechanical deformation.[49] Our previous work has shown that the vertically aligned BFO-BTO micropillar structure can enhance the piezoelectric response of P(VDF-TrFE), and that varying the micropillar aspect ratio can regulate the strain distribution and consequently influence the output performance.[50] However, although structured inorganic/polymer composites exhibit promising electromechanical properties, the effects of key microstructural parameters on interfacial interactions and the underlying physical mechanisms governing polarization and piezoelectric response have yet to be systematically clarified.

Natural cicada wings possess highly ordered protrusion arrays that form localized contacts with bacterial cell membranes, inducing membrane stretching and deformation while generating large local strains that ultimately cause membrane rupture. Inspired by this natural structure and mechanism, we developed a microcone-array engineering strategy to enhance piezoelectric performance.[51] To implement this strategy, lead-free 0.7BFO–0.3BTO (BFO–BTO) pyramidal microcone arrays of varying heights were fabricated on P(VDF-TrFE) films *via* an AAO template-assisted method. These microcones promote β-phase transformation of P(VDF-TrFE) and enable efficient strain transfer to the underlying polymer layer. Systematic studies reveal that microcone height significantly influences polarization behavior, piezoelectric coefficient, and electrical output, with an optimal height of 1.5 μm that balances enhanced piezopotential against structural collapse. The resulting flexible device exhibits excellent sensing and energy-harvesting performance with good operational stability. This work provides rational design guidelines for next-generation piezoelectric composite films in sensing, energy harvesting, and wearable electronics.

Experimental

2.1 Preparation of BFO–BTO Microcone/P(VDF-TrFE) Composite Films

The BFO-BTO microcone structures were fabricated using a commercial tapered-pore anodic aluminum oxide (AAO) template-assisted method. The bottom diameter of the tapered pores in the selected AAO template was approximately 450 nm, with a tip-to-tip spacing of around 450 nm. The pore depths were set at 0.4, 0.9, 1.5, 2.5, and 3 μm, respectively, to obtain microcone arrays of different heights.

First, the precursor solution for 0.7BFO-0.3BTO was prepared as described in our previous work,[50] and the as-prepared BFO-BTO precursor sol was uniformly deposited onto the surface of the AAO template by spin coating. The spin-coating speed was set at 4000 rpm for 60 s to ensure thorough infiltration of the sol into the template pores *via* capillary action. Subsequently, the samples were subjected to a short-term heat treatment at 300 °C for 5 min to accelerate solvent evaporation and promote the sol-to-gel transition. To further enhance pore filling density and structural integrity, the spin-coating and preheating steps were repeated five times. Finally, the samples were annealed in a tube furnace at 550 °C for 5 h to achieve full crystallization of BFO-BTO and optimize its piezoelectric performance.

After completing the inorganic microcone fabrication, the P(VDF-TrFE) polymer functional layer was prepared by spin coating. The copolymer, with a PVDF/TrFE molar ratio of 70:30, was dissolved in N,N-dimethylformamide (DMF) at a concentration of 10 wt%. The solution was heated and stirred at 60 °C for 3 h to ensure complete dissolution and formation of a homogeneous and stable solution. Subsequently, the solution was spin-coated onto the surface of the AAO template filled with BFO-BTO microcones and dried in a vacuum oven at 120 °C for 4 h, yielding a dense and uniform composite film.

To obtain a self-supporting BFO-BTO microcone/P(VDF-TrFE) composite membrane, the AAO template was

Just Accepted

completely removed. First, the aluminum substrate at the bottom of the template was dissolved using a mixed etchant composed of 20 wt% $CuCl_2$ and 10 wt% HCl for 20 h, ensuring complete removal of the aluminum. Subsequently, the sample was immersed in 10 wt% NaOH solution for 8 h to dissolve the AAO template and release the BFO-BTO microcone/P(VDF-TrFE) composite structure. Finally, the samples were thoroughly rinsed with deionized water several times and dried at room temperature. After this procedure, BFO-BTO/P(VDF-TrFE) composite films with microcone heights of 0.4, 0.9, 1.5, 2.5, and 3 μm were successfully prepared. The prepared composite piezoelectric films are shown in Fig. S1. The as-prepared piezoelectric films were subsequently encapsulated with polydimethylsiloxane (PDMS). The encapsulated device was subsequently immersed in silicone oil preheated to 120 °C and poled under a DC electric field of 120 kV cm^{-1} for 1 h using a high-voltage DC power supply (ET2673D-4).

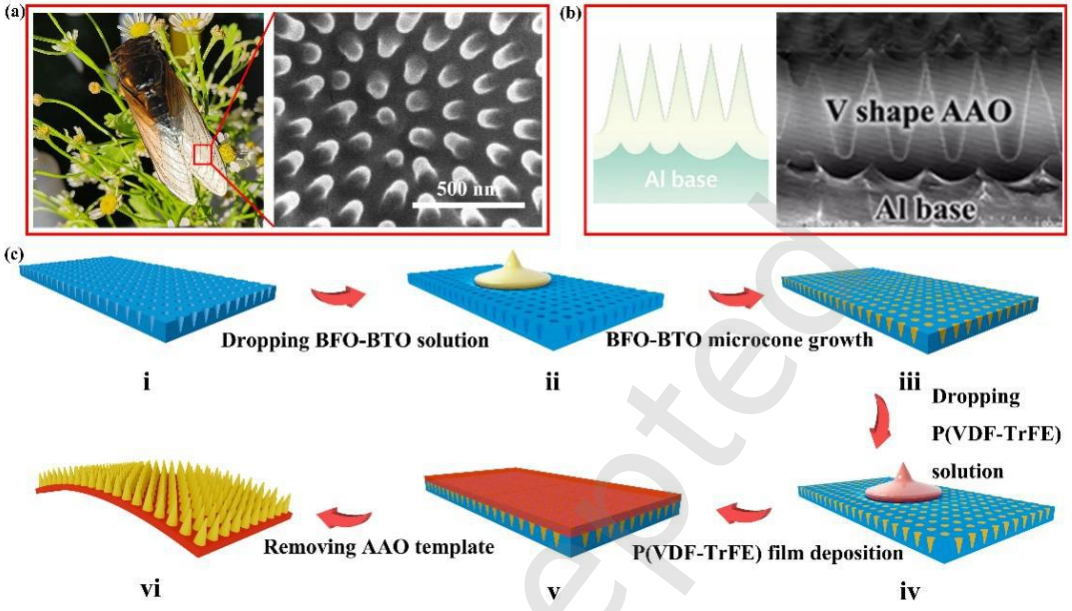


Figure 1 (a) Optical image of a natural cicada and SEM image of its wing surface. (b) Schematic diagram of the microstructure and SEM image of the V-shaped pore AAO template structure (SEM image of the AAO template courtesy of Shenzhen Topology Fine Film Technology, used with permission). (c) Schematic illustration of the fabrication process of the BFO-BTO microcone/P(VDF-TrFE) composite film.

2.2 Characterization

The crystal structure and phase composition of the samples were first examined using an X-ray diffractometer (XRD, Bruker D8). The polymer molecular conformation and the formation of the piezoelectric-active *β* phase were subsequently analyzed within the wavenumber range of 600-1500 cm^{-1} by Fourier transform infrared spectroscopy (FTIR, Nicolet IS50). The surface morphology and microstructural features of the films were observed using a field emission scanning electron microscope (FESEM ZEISS Gemini300). The *P-E* hysteresis loops of the samples were measured using a ferroelectric tester (Trek Model 609B, Trek), while the dielectric properties were characterized using an impedance analyzer (HP4294A, Hewlett-Packard). An atomic force microscope (AFM, Bruker Dimension Icon) was used to investigate local domain patterns, with ±10 V driving voltages applied at the tip. In addition, the stress distribution and electric potential evolution within the device were simulated numerically using the multiphysics simulation software COMSOL. Finally, the output voltage signals generated by the device under external mechanical excitation were recorded in real time using a digital oscilloscope (UTD2102CEX+, UNI-T).

Results and discussion

Inspired by the highly ordered surface microstructure of cicada wings (Fig. 1(a)), we designed and fabricated an ordered BFO-BTO microcone/P(VDF-TrFE) composite film. As shown in Fig. 1(b), the AAO template features V-shaped tapered pores with narrow tips pointing downward toward the underlying Al substrate and wider openings at the top. These tapered pores enable the formation of vertically aligned BFO-BTO microcones with well-defined heights and spacing, thereby translating the ordered surface architecture observed in cicada wings into a controllable inorganic/polymer composite structure. The top surface of the template serves as the deposition interface for the BFO-BTO precursor and guides the formation of well-aligned microcones. Fig. 1(c) illustrates the fabrication process of the BFO-BTO microcone/P(VDF-TrFE) composite film. As shown in Fig. 1(c)(i-iii), the BFO-BTO precursor solution was infiltrated into the pores of the AAO template through capillary action, followed by annealing to ensure complete crystallization, thereby forming BFO-BTO microcones. Subsequently, the P(VDF-TrFE) solution was spin-coated onto the AAO template filled with BFO-BTO microcones (Fig. 1(c-iv)) and after solvent evaporation, a continuous P(VDF-TrFE) layer was formed on the template surface (Fig. 1(c-v)). The AAO template was then removed by chemical etching, yielding the BFO-BTO microcone/P(VDF-TrFE) composite film (Fig. 1(c-vi)); the detailed procedure is provided in the Experimental Section.

To observe the designed microstructure, the top surface of the BFO-BTO microcone/P(VDF-TrFE) composite film was examined by scanning electron microscopy (SEM), as shown in Fig. 2(a–e). The top-view SEM images clearly demonstrate that the BFO-BTO microcone structures were successfully fabricated on the P(VDF-TrFE) matrix using the AAO template-assisted method. For samples with designed microcone heights of 0.4, 0.9, 1.5, 2.5, and 3 μm, distinct and well-defined microcone features are clearly visible on the composite film surface, indicating a high degree of structural

Just Accepted

regularity and uniformity. These results confirm the successful fabrication of microstructured BFO-BTO/P(VDF-TrFE) composite piezoelectric films with precisely tunable microcone geometries. As shown in Fig. 2(c), the 1.5 μm BFO-BTO microcone/P(VDF-TrFE) composite film exhibits an ordered microcone array similar to that of the natural cicada wing, with uniform diameters and well-defined tip morphologies. No obvious agglomeration or collapse is observed, which is conducive to achieving a uniform stress distribution.

The cross-sectional SEM image and its enlarged view are shown in Fig. 2(f) and Fig. 2(g), respectively. The actual height of the microcones is confirmed to be 1.5 μm, while the thickness of the underlying P(VDF-TrFE) film is approximately 40 μm. The vertical orientation and self-supporting characteristics of the microcones can also be verified from these images. Moreover, no obvious pores or interfacial delamination are observed in the cross-sectional image, indicating that intimate physical contact is formed between the BFO-BTO microcones and the P(VDF-TrFE) matrix, which facilitates efficient transfer of externally applied compressive stress throughout the composite film.

To further examine the composition and uniformity of the microcones, energy-dispersive X-ray spectroscopy (EDS) mapping was conducted (Fig. 2(h–l)). The elemental distribution maps clearly reveal that the characteristic elements, including Fe, Bi, Ba, Ti, and O, are homogeneously distributed throughout the microcone regions, with no discernible enrichment or segregation, confirming the excellent compositional uniformity of the BFO-BTO microcones.

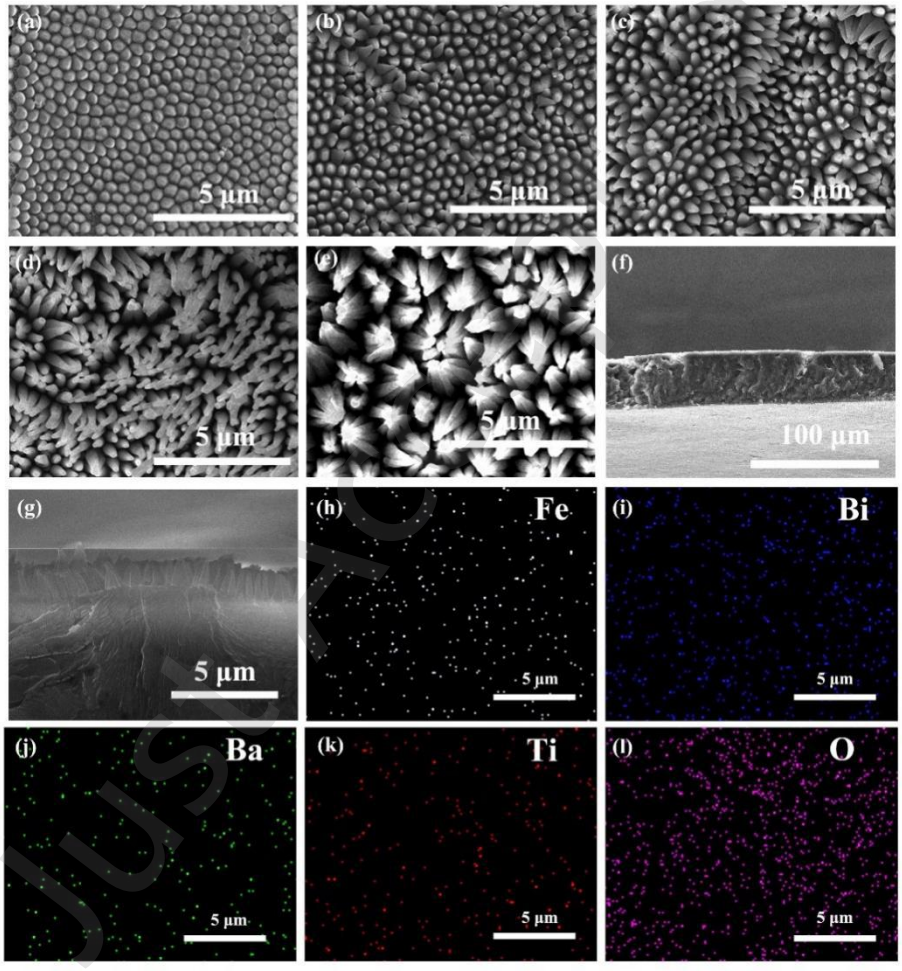


Figure 2 Top-view SEM images of BFO-BTO microcone/P(VDF-TrFE) composite piezoelectric films: (a) 0.4 μm, (b) 0.9 μm, (c) 1.5 μm, (d) 2.5 μm, and (e) 3 μm. (f, g) Cross-sectional SEM image and corresponding enlarged view of the 1.5 μm BFO-BTO microcone/P(VDF-TrFE) composite film. (h-l) Elemental distribution maps of the 1.5 μm BFO-BTO microcones: (h) Fe, (i) Bi, (j) Ba, (k) Ti, and (l) O.

Fig. 3(a) and Fig. 3(b) present the X-ray diffraction (XRD) patterns and Fourier transform infrared (FTIR) spectra, respectively, of the composite films containing BFO-BTO microcones with different heights. The XRD patterns reveal that characteristic diffraction peaks corresponding to both the BFO-BTO phase and the P(VDF-TrFE) polymer phase are simultaneously present in the composite films, indicating the successful formation of a composite structure while preserving the crystalline integrity of both constituent phases. For comparison, the XRD pattern of pure P(VDF-TrFE) is provided in Fig. S2.

In the FTIR spectra, the absorption peaks observed at approximately 846, 1290, and 1431 cm^{-1} are attributed to the β phase of P(VDF-TrFE), confirming the effective formation of this electroactive phase within the composite films. The relative content of the β phase can be calculated based on the Lambert–Beer law,[52] as shown in Eq. (1):

$$F(\beta)=\frac{A_\beta}{\left(\frac{K_\beta}{K_\alpha}\right)A_\alpha+A_\beta}\#(1)$$

where K_α (6.1×10^4 cm^2 mol^{-1}) and K_β (7.7×10^4 cm^2 mol^{-1}) represent the absorption coefficients of the α and β phases, respectively, while A_α and A_β correspond to the absorption peak intensities at 763 and 846 cm^{-1}, respectively. The corresponding results are presented in Fig. 3(c). Compared to pure P(VDF-TrFE), the incorporation of BFO-BTO microcones with lower heights leads to a slight increase in the fraction of the β phase. This increase is attributed to the interfacial interaction between BFO-BTO and P(VDF-TrFE), which may favor the ordered arrangement of polymer chains and thereby promote the formation of the electroactive β phase, consistent with previous reports on inorganic nanowire-induced β-phase formation and chain orientation in P(VDF-TrFE).[52,53] However, when the height of the BFO-BTO microcones increases to 2.5 and 3 μm, the β-phase content decreases instead. This reduction may be attributed to the higher aspect ratio, which can cause the microcones to undergo structural deformation or even collapse, thereby reducing the effective contact area between BFO-BTO and P(VDF-TrFE), as demonstrated in Fig. S3.

Fig. 3(d) compares the piezoelectric coefficient d_{33} of the pure P(VDF-TrFE) film and the BFO-BTO microcone/P(VDF-TrFE) composite films with different microcone heights. The d_{33} value does not increase monotonically with increasing microcone height. Instead, it reaches a maximum value of approximately 19 pC N^{-1} at a microcone height of 1.5 μm.

To understand this non-monotonic behavior, the piezoelectric response can be considered a synergistic result of the intrinsic piezoelectric activity of the constituent materials and the efficiency of mechanical stress transfer within the composite structure. According to the piezoelectric constitutive relationship:[54]

$$D = dT + \varepsilon^T E\#(2)$$

where D represents the electric displacement, d is the piezoelectric coefficient, T is the applied mechanical stress, ε^T is the dielectric permittivity under constant stress, and E is the electric field, the influence of microcone height h on the apparent piezoelectric coefficient of the present system can be understood from two aspects. At the mechanical level, a stress gradient develops along the cone height under the same applied force F, stress concentrates at the top while being dispersed toward the bottom. Based on axial force conservation, the effective axial stress can be approximated as (see Supporting Note S1 for the detailed derivation)[55]:

$$T(z)=\frac{F}{A(z)}, A(z)=A_{top}\left(1+z\,\frac{tan\theta}{r_{top}}\right)^2\#(3)$$

where $T(z)$ is the axial stress at position z, $A(z)$ is the cross-sectional area at position z, A_{top} is the tip cross-sectional area, r_{top} is the tip radius, and θ is the sidewall inclination angle. Here, z is measured from the tip toward the base. As z increases, $A(z)$ gradually increases, resulting in a decrease in the local axial stress $T(z)$ and thus a stress concentration near the tip. When the microcone height h is relatively small, the resulting low aspect ratio (height-to-diameter ratio) limits the geometric variation and stress concentration, leading to insufficient stress transfer. Increasing h increases the aspect ratio, thereby enhancing stress concentration and interfacial stress transfer. However, an excessively high aspect ratio compromises the structural stability of the microcones, making them more susceptible to bending, tilting, or partial collapse under external loading and consequently reducing the effective stress transfer. At the composite-structure level, the height directly determines the ceramic volume fraction ϕ_c, which in turn affects d. Increasing h linearly raises ϕ_c, which enhances the ceramic contribution and thus gradually elevates d toward the pure ceramic value. However, the polymer phase serves as the flexible matrix. If h becomes too large, resulting in an excessively high ϕ_c, the flexibility of the composite film deteriorates, and interfacial defects become more prevalent, ultimately causing a decline in d. Therefore, there exists an optimal sample that maximizes stress transfer to the ceramic phase while remaining within the mechanical strength limit of the structure.

Fig. 3(e) shows the polarization–electric field (P–E) hysteresis loops measured for pure P(VDF-TrFE) and BFO-BTO/P(VDF-TrFE) composite films with microcone heights of 0.4, 0.9, 1.5, 2.5, and 3 μm at 10 Hz. Clearly, the 1.5 μm BFO-BTO/P(VDF-TrFE) composite film exhibits the highest remanent polarization (P_r) of 13.3 μC cm^{-2} under an applied electric field of 150 MV m^{-1}. In comparison, the P_r values of the 0.4, 0.9, 2.5, and 3 μm BFO-BTO/P(VDF-TrFE) composite films and pure P(VDF-TrFE) under the same conditions are 8.9, 11.8, 6.3, 5.4, and 1.9 μC cm^{-2}, respectively. These results demonstrate that the incorporation of BFO-BTO microcones significantly enhances the ferroelectric properties of the composite films, with the enhancement depending strongly on the microcone height.

Fig. 3(f) presents the corresponding maximum polarization (P_{max}) values. At an electric field of 150 MV m^{-1}, the P_{max} of the composite film with a microcone height of 1.5 μm reaches 24.3 μC cm^{-2}, whereas the P_{max} values of the 0.4, 0.9, 2.5, and 3 μm composite films and pure P(VDF-TrFE) are 16.1, 19.1, 11.92, 11.98, and 6.52 μC cm^{-2}, respectively. These results indicate that P_{max} initially increases with increasing microcone height and reaches a maximum at 1.5 μm, followed by a decrease at higher microcone heights. The enhancement of polarization is primarily attributed to the interface polarization effect, which is amplified as the microcone height increases. However, when the microcone height exceeds 1.5 μm, the higher aspect ratio may induce slight deformation or collapse of the microcones, thereby compromising the effective interface and limiting the polarization enhancement.

Just Accepted

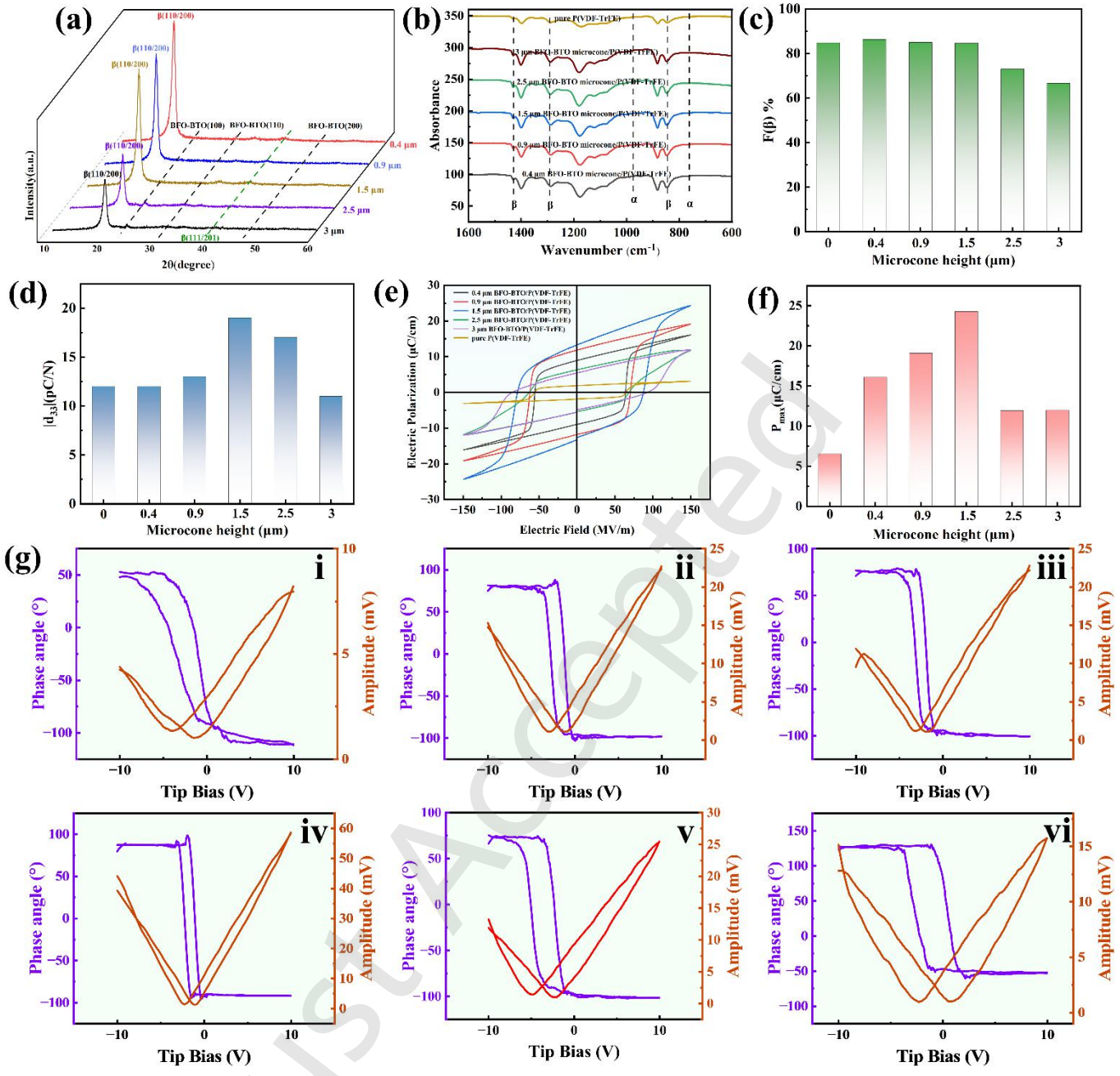


Figure 3 Structural and ferroelectric/piezoelectric performance characterization of BFO-BTO microcone/P(VDF-TrFE) composite films with different microcone heights (0.4, 0.9, 1.5, 2.5, and 3 μm). (a) X-ray diffraction (XRD) patterns of the composite films. (b) Fourier transform infrared (FTIR) spectra. (c) Calculated relative *β*-phase content in P(VDF-TrFE) derived from the FTIR spectra. (d) Comparison of the piezoelectric coefficient d_{33} of the composite films. (e) Polarization-electric field (*P-E*) hysteresis loops of composite films with different microcone heights. (f) Statistical bar chart of the maximum polarization (P_{max}). (g) PFM phase and amplitude hysteresis loops of pure P(VDF-TrFE) (i) and BFO-BTO microcone/P(VDF-TrFE) composite films with different microcone heights of (ii) 0.4, (iii) 0.9, (iv) 1.5, (v) 2.5, and (vi) 3 μm.

To further investigate the local piezoelectric responses of the composite films, piezoresponse force microscopy (PFM) measurements were performed. As shown in Fig. 3(g), the pure P(VDF-TrFE) film exhibits a relatively weak amplitude response, indicating a limited local electromechanical response. After introducing the BFO-BTO microcone arrays, all composite films exhibit enhanced phase contrast and amplitude signals, confirming the improved local piezoelectric response resulting from the incorporation of the inorganic ceramic microstructures. Notably, the 1.5 μm BFO-BTO microcone/P(VDF-TrFE) composite exhibits the highest amplitude response among all samples, indicating the strongest electromechanical response. This finding corroborates the d_{33} test results.

To ensure firm adhesion and reliable electrical contact between the electrodes and the piezoelectric film, copper foils coated with conductive acrylic rubber were employed as the top and bottom electrodes (Fig. 4(a-ii)). This electrode configuration provides stable electrical contact while maintaining good mechanical coupling with the piezoelectric

Just Accepted

layer. To provide reliable encapsulation and ensure the biocompatibility of the device, PDMS, a nontoxic and biocompatible polymer, was employed as the encapsulation layer. The piezoelectric performance of the BFO-BTO microcone/P(VDF-TrFE) composite films with different microcone heights, together with that of the pure P(VDF-TrFE) film, was evaluated using a piezoelectric signal acquisition system. As shown in Fig. 4(b), under a constant external force of 0.66 N at 5 Hz, the output voltage exhibits a non-monotonic dependence on the BFO-BTO microcone height, initially increasing and then decreasing. This variation is consistent with the trend in the piezoelectric coefficient, d_{33}. Among all samples, the device with a microcone height of 1.5 μm delivers the highest piezoelectric output, with a maximum open-circuit voltage (V_{OC}) of approximately 5.12 V. Further increasing the microcone height results in a gradual decrease in the output voltage.

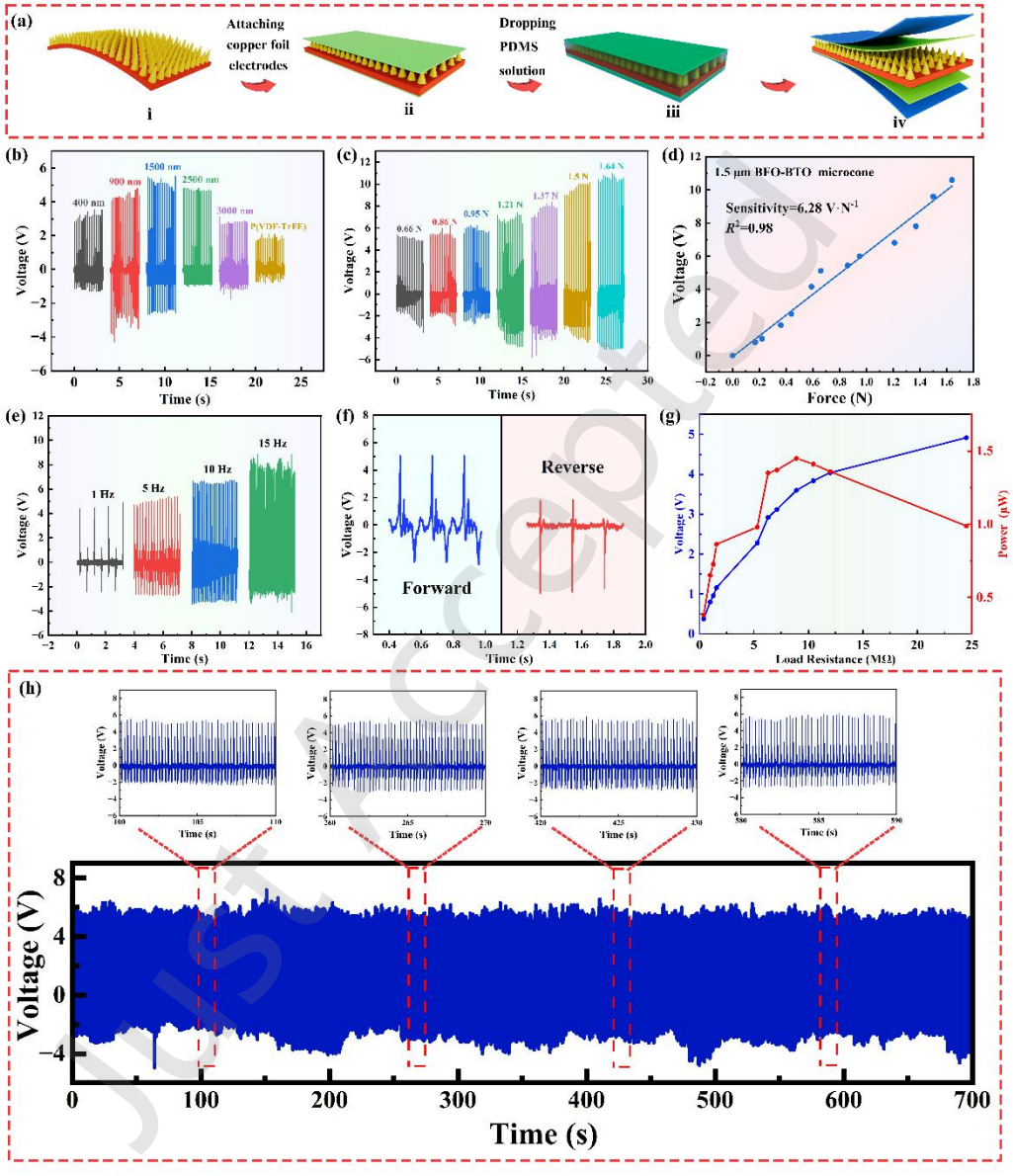


Figure 4 Characterization of the piezoelectric output performance of 1.5 μm BFO-BTO microcone/P(VDF-TrFE) composite film. (a) Schematic illustration of the fabrication process of the BFO-BTO microcone/P(VDF-TrFE) based piezoelectric device. (b) Output voltage comparison between composite films with different microcone heights and the pure P(VDF-TrFE) film under the same external force. (c) Output voltage of the 1.5 μm composite film under different applied forces. (d) Corresponding force sensitivity of the output voltage. (e) Variation of output voltage with impact frequency. (f) Comparison of output voltage under forward and reverse connection conditions. (g) Output voltage as a function of external load resistance and the corresponding peak power. (h) Stability of open-circuit output voltage under long-term repetitive tapping.

As shown in Fig. 4(c), at a fixed excitation frequency of 5 Hz, the output voltage of the 1.5 μm BFO-BTO/P(VDF-TrFE) device increases progressively with increasing applied force in the range of 0.66–1.64 N. A clear linear relationship between the peak output voltage and the applied force is observed, as confirmed by linear fitting (Fig. 4(d)), yielding a force sensitivity of 6.28 V·N^{-1} and a high linearity of R^2 = 0.98. Although its piezoelectric coefficient and output voltage are

Just Accepted

comparable to, rather than exceeding, those of several reported composites (Table S1),[50,56-69] the BFO-BTO/P(VDF-TrFE) microcone system exhibits the highest sensitivity (6.28 $V \cdot N^{-1}$), surpassing even the PZT micropillar-based composite (3.52 $V \cdot N^{-1}$).[56] Moreover, compared with the micropillar structure of the same composition and height in our previous work,[50] its piezoelectric coefficient, output voltage, and sensitivity are further enhanced, mainly due to the graded microcone geometry, which optimizes stress distribution and enhances local stress concentration.

Fig. 4(e) further demonstrates that the output voltage increases monotonically with increasing impact frequency from 1 to 15 Hz. This behavior can be attributed to the increased number of mechanical deformation cycles per unit time at higher excitation frequencies, which promotes faster charge generation and transfer through the external circuit, thereby resulting in an enhanced output voltage. Fig. 4(f) shows the output voltage of the 1.5 μm BFO-BTO microcone/P(VDF-TrFE) composite device under forward and reverse electrical connections. The nearly identical voltage responses under both connection directions confirm consistent piezoelectric output, and, together with the shielding-layer experiment in Fig. S4, establish that the measured signal is predominantly piezoelectric in origin, with negligible triboelectric contribution. In addition, as shown in Fig. 4(g), the output voltage increases with increasing external load resistance, while the output power reaches a maximum value of approximately 1.45 μW at an optimal load resistance of 8.9 MΩ. This relatively high-power output highlights the potential of the device for powering or supporting low-power electronic components. Furthermore, as shown in Fig. 4(h), the device maintains a stable open-circuit output voltage of approximately 5 V over 3000 tapping cycles. No obvious degradation in the output signal is observed during repeated mechanical deformation, demonstrating the excellent durability and operational stability of the 1.5 μm BFO-BTO/P(VDF-TrFE) composite piezoelectric device.

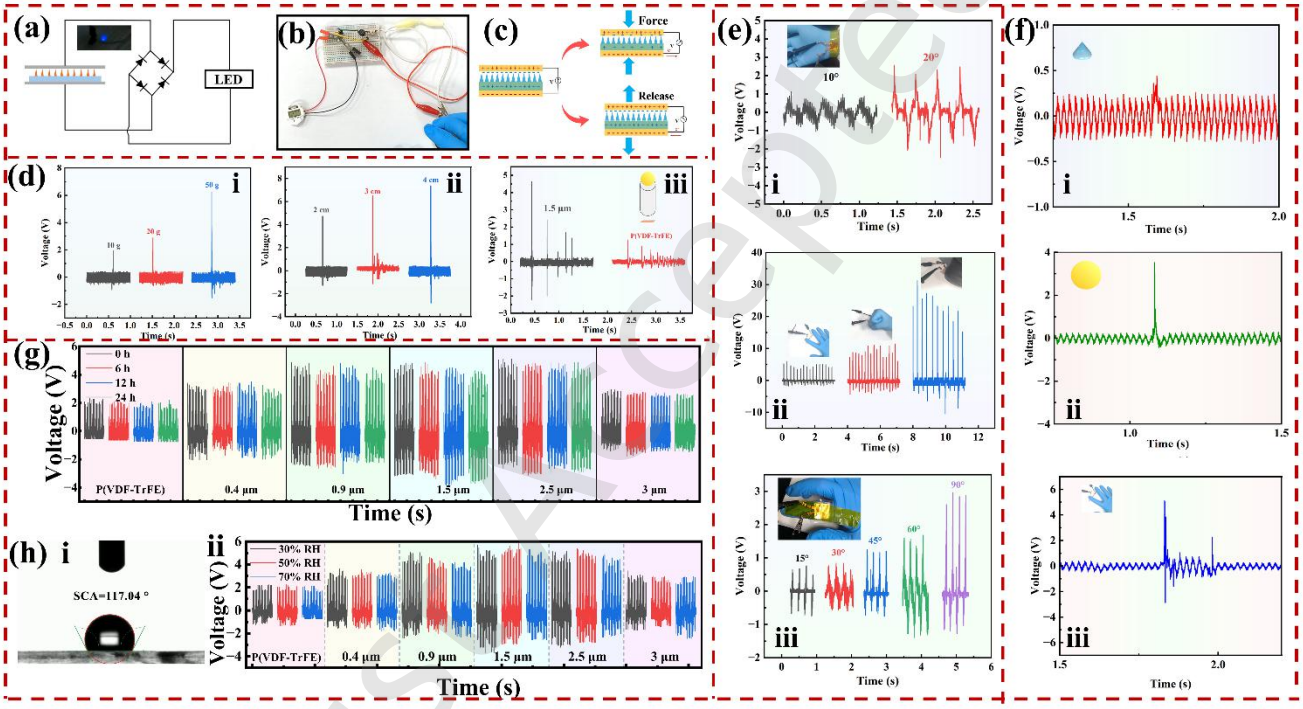


Figure 5 Energy harvesting and sensing performance of the 1.5 μm BFO-BTO/P(VDF-TrFE) composite piezoelectric device. (a) Schematic illustration and photograph of a blue LED lit under fist impact. (b) Capacitor charging and powering a digital watch through a rectifier circuit. (c) Schematic of the piezoelectric response under compression, with corresponding release states. (d) (i) Output signals under different dropped masses from a height of 3 cm; (ii) output signals of a 50 g weight dropped from different heights; (iii) comparison of the output voltage between the composite film and pure P(VDF-TrFE) film under ping-pong ball impact. (e) (i) Wrist-bending response; (ii) dynamic responses to finger tapping, fist impact, and foot stepping; (iii) finger-bending response. (f) (i) Water-droplet impact; (ii) ping-pong ball impact; (iii) finger touch. (g) Moisture-resistance performance of the six devices: output voltage responses after 0, 6, 12, and 24 h of sweat exposure. (h) (i) Static water contact angle of the PDMS encapsulation layer; (ii) Output voltage responses under relative humidities (RH) of 30%, 50%, and 70%.

The energy harvesting capability of the device was further demonstrated through LED illumination and digital watch powering experiments driven by fist impacts, as shown in Fig. 5(a) and 5(b). The 1.5 μm BFO-BTO/P(VDF-TrFE) composite piezoelectric device was placed on a flat surface and directly connected in series with a blue LED. Upon mechanical impact, the generated instantaneous voltage was sufficient to illuminate the blue LED (operating voltage: 2–3 V) without the use of an additional energy storage unit (Fig. 5(a), Video S1). Furthermore, to demonstrate its capability for sustained power delivery, the alternating-current output was converted into direct current using a rectifier circuit and subsequently stored in a capacitor. Once the capacitor was sufficiently charged, the stored electrical energy was released to power a digital watch for an extended period (Fig. 5(b), Video S2).

Fig. 5(c) schematically illustrates the working mechanism of the piezoelectric device under compressive deformation.

Just Accepted

When an external mechanical force is applied, the resulting strain induces a displacement of the dipoles within the piezoelectric material, leading to a change in polarization and the generation of a potential difference between the two electrodes. Consequently, electrons flow through the external circuit to compensate for the induced potential difference, generating an electrical output signal. Upon removal of the external force, the material returns toward its initial state, resulting in a reverse change in polarization and an opposite flow of electrons through the external circuit. This reversible electromechanical conversion process enables the device to continuously convert mechanical energy into electrical energy under cyclic mechanical deformation.

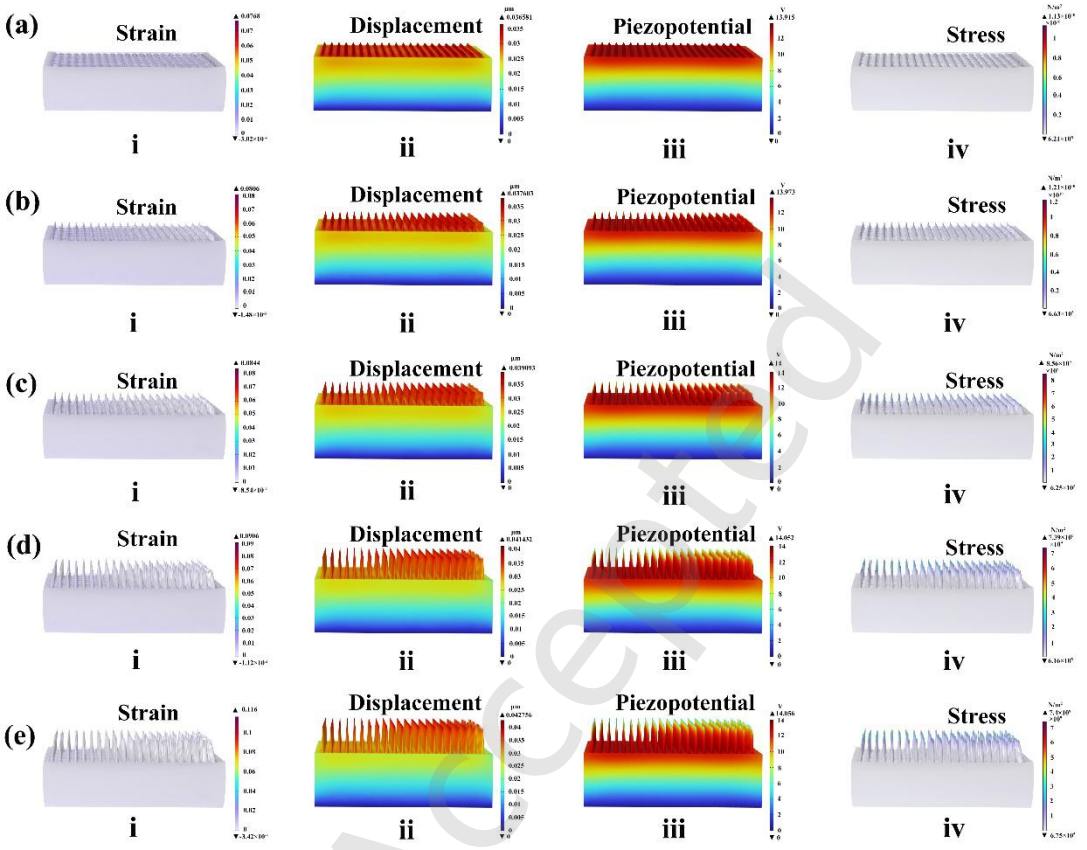


Figure 6 COMSOL simulation results of BFO-BTO microcone/P(VDF-TrFE) composite films: (a) 0.4 μm, (b) 0.9 μm, (c) 1.5 μm, (d) 2.5 μm, and (e) 3 μm microcones; (i) strain distribution, (ii) displacement distribution, (iii) piezoelectric potential distribution, (iv) stress distribution.

Further investigations focused on the electrical signal responses generated by vertically dropping weights with different masses (10, 20, and 50 g) from a fixed height of 3 cm onto the BFO-BTO/P(VDF-TrFE) composite device (Fig. 5(d-i)). The results clearly show that the output voltage amplitude increases with increasing weight mass. This behavior can be attributed to the greater impact force and kinetic energy associated with the heavier weights, which induce larger mechanical deformation in the piezoelectric layer. In addition, a 50 g weight was freely dropped from different heights ranging from 2 to 4 cm. As shown in Fig. 5(d-ii), the output signal increases with increasing dropping height, indicating the capability of the device to distinguish impact stimuli with different intensities.

To further evaluate the capability of the device to detect weak mechanical impacts, the free-fall impact of a ping-pong ball was monitored. As shown in Fig. 5(d-iii), a ping-pong ball with a diameter of 4 cm and a mass of 2.5 g was freely dropped from a height of 30 cm onto the device. The output voltage of the 1.5 μm composite film reaches approximately 4.6 V, compared with only approximately 1.22 V for the pure P(VDF-TrFE) film. This significant enhancement demonstrates that the incorporation of the BFO-BTO microcone structure effectively improves the sensitivity of the composite film to mechanical impacts.

To further demonstrate the sensing performance of the device for human motion monitoring, the sensor was attached to the wrist. As shown in Fig. 5(e-i), the output voltage increases monotonically with increasing wrist bending angle, demonstrating the flexibility of the composite film and its capability to detect wrist movements. Furthermore, to evaluate the ability of the device to distinguish different mechanical stimuli associated with human activities, the BFO-BTO/P(VDF-TrFE) composite film was secured on a flat surface and subjected to periodic impact excitation corresponding to different movements (Fig. 5(e-ii)). Different actions, including finger tapping, fist impact, and foot stepping, generate distinct output signal waveforms due to differences in the applied mechanical stimuli. These characteristic signal profiles enable the differentiation of different motion patterns, while the signal amplitudes provide information about the relative intensity of the applied stimuli. To further demonstrate the potential of the composite film for monitoring finger motion, the sensor was attached to the user's index finger to investigate the relationship between the output voltage and finger bending angle (Fig. 5(e-iii)). The output voltage exhibits a linear dependence on the finger bending angle, further demonstrating the capability of the device for detecting dynamic finger movements. Fig. S5 presents enlarged output

Just Accepted

voltage profiles of the piezoelectric device recorded under different applied pressures, providing a more detailed evaluation of its transient response. The device responds rapidly to each mechanical stimulus, with the peak voltage increasing from approximately 4.5 to 9.6 V as the applied pressure increases from 0.6 N to 1.3 N. Meanwhile, the response time decreases from 15.5 to 13.7 ms, whereas the recovery time increases from 19.4 to 26.3 ms. The faster signal establishment under higher pressure can be related to the increased deformation and more efficient stress transfer within the device. In contrast, the extended recovery process may be associated with enhanced viscoelastic relaxation of the P(VDF-TrFE) matrix after unloading and subsequent charge redistribution within the composite.[70]

Furthermore, the response of the device to mechanical stimuli with different intensities was evaluated using water droplets, ping-pong balls, and finger touching (Fig. 5(f)). The output voltage amplitude increases progressively from the relatively weak impact of a water droplet to the stronger mechanical stimuli generated by a ping-pong ball and finger touching. These results demonstrate the ability of the composite device to respond to a broad range of mechanical stimuli, from weak impacts to direct human contact, highlighting its potential for versatile mechanical and wearable sensing applications. In addition, the moisture resistance of the encapsulated devices was further evaluated under artificial sweat exposure and different ambient humidities. As shown in Fig. 5(g), the output voltage responses of the six devices were recorded after 6, 12, and 24 h of artificial sweat exposure. The devices exhibit relatively stable output signals throughout the exposure period, with no significant decrease in output voltage observed even after 24 h, demonstrating good resistance to sweat. Fig. 5(h-i) shows the static water contact angle of the PDMS encapsulation layer, which was measured to be 117.04°. The relatively large contact angle indicates the hydrophobic nature of the PDMS surface, which helps reduce the penetration and accumulation of moisture on the device surface. Fig. 5(h-ii) presents the output voltage responses of the six devices under relative humidities of 30%, 50%, and 70%. Although the ambient humidity was increased over a relatively wide range, the output voltages remained comparatively stable without obvious fluctuations or degradation. Taken together, these results demonstrate that the PDMS-encapsulated devices possess good environmental stability and can maintain reliable electrical performance under both sweat exposure and varying humidity conditions, supporting their potential for practical wearable sensing applications.

To further correlate the simulated electromechanical behavior with the theoretical model, the output characteristics can be understood in terms of the piezoelectric constitutive relation:[71]

$$V = \frac{d_{33}}{\varepsilon_r} E \varepsilon L (4)$$

where the output voltage is governed by the coupled contributions of material properties and mechanical deformation. Within this framework, the finite element simulation results can be directly linked to variations in the strain (ε) and stress distribution within the composite structure.

To further investigate the electromechanical behavior of the BFO-BTO microcone/P(VDF-TrFE) composites, finite element analysis was performed using COMSOL Multiphysics to evaluate the strain, displacement, stress, and piezoelectric potential distributions of composites with different microcone heights. The simulation results show that the strain, displacement, and piezoelectric potential generally increase with increasing microcone height from 0.4 to 3 μm. At a microcone height of 0.4 μm, the maximum strain reaches 7.68×10^{-2} (Fig. 6(a-i)), which increases to 1.16×10^{-1} at 3 μm (Fig. 6(e-i)). Meanwhile, the displacement also increases progressively with increasing microcone height. At 3 μm, the simulated piezoelectric potential reaches 14.056 V (Fig. 6(e-iii)), which is higher than those obtained for the other microcone heights. Furthermore, the stress distribution reveals that the stress is predominantly concentrated near the apex of the microcones (Fig. 6(a-iv)–(e-iv)), providing direct evidence for the localized stress-concentration effect induced by the pyramidal microcone geometry. This simulation result further supports the proposed mechanism that the microcone structure promotes localized stress concentration and facilitates stress transfer within the piezoelectric composite, thereby contributing to enhanced charge generation and electromechanical response.

From the perspective of the theoretical model, the increase in strain (ε) directly contributes to the enhancement of the output voltage according to the above equation, while the increased deformation amplitude further amplifies the electromechanical coupling efficiency. Notably, the stress initially increases and then decreases with increasing microcone height. Microcones with an appropriate height are beneficial for enhancing the local stress response at the contact interface between the cone base and the P(VDF-TrFE) matrix, enabling the external load to be transferred more effectively to the BFO-BTO microcone structure. However, when the microcone height further increases, the larger aspect ratio may reduce the mechanical stability of the microcones, making them more prone to bending, tilting, or local deformation under external force. As a result, the stress transfer efficiency decreases, and part of the applied load is dispersed by the surrounding polymer matrix. Therefore, an excessive microcone height may compromise both interfacial stress concentration and efficient load transfer, leading to a decrease in the internal stress of the composite films. In brief, as the microcone height increases, the strain, displacement, and piezopotential exhibit a clear positive correlation, which further validates the effectiveness of introducing microcone arrays for improving the piezoelectric performance of the composites.

Conclusion

In this study, a series of BFO-BTO microcone/P(VDF-TrFE) composite flexible piezoelectric films were successfully fabricated using an AAO template-assisted method. By systematically varying the microcone height, the structure–stress–polarization–performance relationship in microcone-array-based inorganic/polymer piezoelectric composites was elucidated. Experimental results showed that the piezoelectric performance strongly depended on the microcone height, with the 1.5 μm microcone array exhibiting the highest output voltage (~5.12 V) and force sensitivity (6.28 $V \cdot N^{-1}$). Finite element simulations further revealed the underlying mechanism: increasing the microcone height markedly enhanced the strain concentration and vertical displacement and consequently increased the piezoelectric potential, highlighting the critical role of microcone geometry in regulating interfacial stress transfer and electromechanical coupling. Based on this optimized architecture, the composite film was employed as a flexible self-powered sensor, showing stable operation over

Just Accepted

3000 mechanical cycles, reliable detection of weak external stimuli such as ping-pong ball impacts and finger tapping, and a linear voltage response to finger bending angle. Overall, this work reveals how microcone geometry governs interfacial stress and polarization, boosting the piezoelectric and sensing performance of flexible piezoelectric composites.

Data availability

The data that support the findings of this study are available from the corresponding author upon reasonable request.

Acknowledgements

The work is supported by the National Natural Science Foundation of China (52302145 and 52502151), the Natural Science Foundation of Shandong Province (ZR2023QE126 and ZR2026MS0844), the Young Talent of Lifting engineering for Science and Technology in Shandong (SDAST2024QTA017), the China Postdoctoral Science Foundation (2025M770099), the Youth Innovation Team Program in Colleges of Shandong Province (2024KJH023), the Natural Science Foundation of Shanghai (25ZR1404008) and the Open Fund of Hubei Key Laboratory of Micro-Nanoelectronic Materials and Devices (K202308). Thanks to the Analytical Testing Center from Shandong University of Technology for the test condition support.

Declaration of competing interest

All the contributing author(s) report(s) no conflict of interests in this work.

Author contribution statement

Wentao Yang: Writing – original draft, Data curation, Formal analysis, Project administration, Methodology. **Hang Zhan:** Writing – original draft, Data curation, Software, Formal analysis, Investigation, Validation. **Panpan Lv:** Writing – review and editing, Formal analysis, Methodology, Conceptualization. **Guiyun Gao**: Project administration, Methodology. **Shuzhi Zhang:** Project administration, Methodology. **Le Xin:** Writing – review and editing. **Cuncheng Li**: Visualization, Software. **Luchao Ren:** Visualization, Software. **Jin Qian:** Resources, Supervision, Formal analysis, Methodology. **Mingwei Zhang:** Resources, Supervision, Formal analysis, Methodology.

Informed consent

Not applicable.

Ethics statement

Not applicable.

Use of AI statement

None.

Reference

[1] Ellabban O., Abu-Rub H., Blaabjerg F. Renewable energy resources: Current status, future prospects and their enabling technology. *Renewable and Sustainable Energy Reviews*, **2014**, 39, 748–764.

[2] Panwar N. L., Kaushik S. C., Kothari S. Role of renewable energy sources in environmental protection: A review. *Renewable and Sustainable Energy Reviews*, **2011**, 15, 1513–1524.

[3] Rahman A., Farrok O., Haque M. M. Environmental impact of renewable energy source based electrical power plants: Solar, wind, hydroelectric, biomass, geothermal, tidal, ocean, and osmotic. *Renewable and Sustainable Energy Reviews*, **2022**, 161, 112279.

[4] Mohseni S., Brent A. C. Long-term planning optimisation of sustainable energy systems: A systematic review and meta-analysis of trends, drivers, barriers, and prospects. *Energy Strategy Reviews*, **2025**, 57, 101640.

[5] Emodi N. V., Wade B., Rekker S., Greig C. A systematic review of barriers to greenfield investment in decarbonisation solutions. *Renewable and Sustainable Energy Reviews*, **2022**, 165, 112586.

[6] Zhang H., Chen Y. R., Deng Z. K., Deng L., Xing J. C., Yang Q. L., Mi H. J., Zhang H. T., Xu C. H., Shen X. D., Yang J., Xie L. Q. A high-output performance disc-shaped liquid-solid triboelectric nanogenerator for harvesting omnidirectional ultra-low-frequency natural vibration energy. *Nano Energy*, **2024**, 121, 109243.

[7] Manchi P., Graham S. A., Patnam H., Alluri N. R., Kim S.-J., Yu J. S. $LiTaO_3$- Based Flexible Piezoelectric Nanogenerators for Mechanical Energy Harvesting. *ACS Applied Materials & Interfaces*, **2021**, 13, 46526–46536.

[8] Qi Y. C., Liu G. X., Gao Y. Y., Bu T. Z., Zhang X. H., Xu C. Q., Lin Y., Zhang C. Frequency Band Characteristics of a Triboelectric Nanogenerator and Ultra-Wide-Band Vibrational Energy Harvesting. *ACS Applied Materials & Interfaces*, **2021**, 13, 26084–26092.

[9] Tang W., Sun Q. J., Wang Z. L. Self-Powered Sensing in Wearable Electronics-A Paradigm Shift Technology. *Chemical Reviews*, **2023**, 123, 12105–12134.

[10] Teng F. R., Sun S., Tan S. C., Ma Y. J., Huang Y., Zhu L., Wu D., Li A.-D. Multifunctional flexible multilayer pressure sensor for pressure sensing, energy harvesting and versatile applications. *Chemical Engineering Journal*, **2025**, 522, 166937.

[11] Jiang Q. H., Antwi-Afari M. F., Fadaie S., Mi H.-Y., Anwer S., Liu J. Self-powered wearable Internet of Things sensors for human-machine interfaces: A systematic literature review and science mapping analysis. *Nano Energy*, **2024**, 131, 110252.

[12] Wu T., Lu Y., Tao X., Chen P., Zhang Y., Ren B., Xie F., Yu X., Zhou X., Yang D. Superelastic wood‐based nanogenerators magnifying the piezoelectric effect for sustainable energy conversion. *Carbon Energy*, **2024**, 6, e561.

[13] Sun T.-W., Venkatesan M., Hsu Y.-C., Chandrasekar J., Chen W.-C., Bénas J.-S., Cho C.-J., Lin J.-H., Liang F.-C., Rwei A. Y. MXene-reinforced water insensitive self-healing piezoelectric nanogenerator for ambient and aquatic mechano-pressure sensing. *Nano Energy*, **2025**, 133, 110416.

[14] Jean F., Khan M. U., Alazzam A., Mohammad B. Advancement in piezoelectric nanogenerators for acoustic energy harvesting. *Microsystems & Nanoengineering*, **2024**, 10, 197.

[15] Das K. K., Basu B., Maiti P., Dubey A. K. Piezoelectric nanogenerators for self‐powered wearable and implantable bioelectronic devices. *Acta biomaterialia*, **2023**, 171, 85–113.

[16] Chen S., Tong X., Huo Y., Liu S., Yin Y., Tan M. L., Cai K., Ji W. Piezoelectric biomaterials inspired by nature for applications in biomedicine and nanotechnology. *Advanced Materials*, **2024**, 36, 2406192.

[17] Ali M., Hoseyni S. M., Das R., Awais M., Basdogan I., Beker L. A flexible and biodegradable piezoelectric‐based wearable sensor for non‐invasive monitoring of dynamic human motions and physiological signals. *Advanced Materials Technologies*, **2023**, 8, 2300347.

[18] He Q. R., Briscoe J. Piezoelectric Energy Harvester Technologies: Synthesis, Mechanisms, and Multifunctional Applications. *ACS Applied Materials & Interfaces*, **2024**, 16, 29491–29520.

[19] Pan X., Wu Y. Y., Wang Y. F., Zhou G., Cai H. L. Mechanical energy harvesting based on the piezoelectric materials: Recent advances and future perspectives. *Chemical Engineering Journal*, **2024**, 497, 154249.

[20] Xu T., Jin L., Ao Y., Zhang J., Sun Y., Wang S., Qu Y., Huang L., Yang T., Deng W. All-polymer piezo-ionic-electric electronics. *Nature Communications*, **2024**, 15, 10876.

[21] Xiong J., Wang L., Liang F., Li M., Yabuta Y., Iqbal M. A., Mayakrishnan G., Shi J., Kim I. S. Flexible piezoelectric sensor based on two-dimensional topological network of PVDF/DA composite nanofiber membrane. *Advanced Fiber Materials*, **2024**, 6, 1212–1228.

[22] Ren Z., Deng S., Shao J., Si Y., Zhou C., Luo J., Wang T., Li J., Li J., Liu H. Ultrahigh-power-density flexible piezoelectric energy harvester based on freestanding ferroelectric oxide thin films. *Nature Communications*, **2025**, 16, 3192.

[23] Zheng Z. F., Wang X. C., Hang G. G., Duan J., Zhang J., Zhang W. J., Liu Z. Recent progress on flexible poly(vinylidene fluoride)-based piezoelectric nanogenerators for energy harvesting and self-powered electronic applications. *Renewable and Sustainable Energy Reviews*, **2024**, 193, 114285.

[24] Bian L., Qi X. D., Li K., Fan J. H., Li Z. M., Sun E. W., Yang B., Dong S. X., Cao W. W. High-performance $Pb(Ni_{1/3}Nb_{2/3})O_3$-$PbZrO_3$-$PbTiO_3$ ceramics with the triple point composition. *Journal of the European Ceramic Society*, **2021**, 41, 6983–6990.

[25] Gao B., Yao Z. H., Lai D. Y., Guo Q. H., Pan W. G., Hao H., Cao M.

Just Accepted

H., Liu H. X. Unexpectedly high piezoelectric response in Sm-doped PZT ceramics beyond the morphotropic phase boundary region. *Journal of Alloys and Compounds*, **2020**, 836, 155474.
[26] Tina G. A., Punetha P., Adhikary G. D., Ranjan R. Simultaneous increase in piezoelectric response and Curie point in $BaTiO_3$ based Pb-free piezoceramic. *Scripta Materialia*, **2024**, 243, 115994.
[27] Du Q. P., Zhang C., Liu C. L., Zhou W. J., Zeng F. F., Li K. H., Zou K. L., Fan G. F., Jiang S. L., Fu Q. Y., Wu J. M., Zhang G. Z. Highly <001>-textured $BaTiO_3$ ceramics with high piezoelectric performance prepared by vat photopolymerization. *Additive Manufacturing*, **2023**, 66, 103454.
[28] Habib M., Tang L., Xue G. L., Zhou X. F., Zhang D. Improvement in piezoelectric performance of the lead-free $BiFeO_3$-$BaTiO_3$ ceramics by synergistic approach. *Journal of Materials Science & Technology*, **2023**, 160, 55–65.
[29] Huang Y. Y., Zhang L. Y., Jing R. Y., Yang Y., Shur V., Wei X. Y., Jin L. Superior piezoelectric performance with high operating temperature in bismuth ferrite-based ternary ceramics. *Journal of Materials Science & Technology*, **2024**, 169, 172–181.
[30] Meng K., Li W., Tang X.-G., Liu Q.-X., Jiang Y.-P. A review of a good binary ferroelectric ceramic: $BaTiO_3$–$BiFeO_3$. *ACS Applied Electronic Materials*, **2022**, 4, 2109–2145.
[31] Yan J.-K., Dai J.-Q., Zhang C.-Z., Li Y.-H. Enhanced ferroelectric and piezoelectric properties of Al-doped BiFeO3-BaTiO3 ceramics synthesized via the sol-gel method. *Materials Today Communications*, **2025**, 44, 111856.
[32] Zhang Z. M., Wang Z. Q., Li X. M., Zheng Y., Yang Z. B. Design and Manufacturing of Piezoelectric Biomaterials for Bioelectronics and Biomedical Applications. *Chemical Reviews*, **2025**, 125, 9875–9929.
[33] Li B. M., Ju B., Zhou Y., Knowles C. G., Rosenberg Z., Flewwellin T. J., Kose F., Jur J. S. Airbrushed PVDF–TrFE Fibrous Sensors for E‐Textiles. *ACS Applied Electronic Materials*, **2021**, 3, 5307–5326.
[34] Coondoo I., Isfahani V. B., Amorín H., Bdikin I., Carvalho J., Pascual-González C., Silva B. M., Oliveira J., Pukazhselvan D., Almeida B. G., Miranda G. Flexible and multifunctional P(VDF-TrFE)/BT-BMT polymer composite films: Realizing high piezoelectric performance and electrocaloric effect. *Chemical Engineering Journal*, **2025**, 505, 158639.
[35] Dutta B., Kar E., Bose N., Mukherjee S. NiO@SiO_2/PVDF: A Flexible Polymer Nanocomposite for a High Performance Human Body Motion-Based Energy Harvester and Tactile e‐Skin Mechanosensor. *ACS Sustainable Chemistry & Engineering*, **2018**, 6, 10505–10516.
[36] Chai B., Shi K. M., Wang Y. L., Liu Y. J., Liu F., Zhu L., Huang X. Y. Integrated Piezoelectric/Pyroelectric Sensing from Organic–Inorganic Perovskite Nanocomposites. *ACS Nano*, **2024**, 18, 25216–25225.
[37] Zhao J., Zheng M. P., Gao X., Zhu M. K., Hou Y. D. High-performance flexible piezocomposites based on an enhanced interfacial polarization effect via BCZT@Ag heterostructure design. *Journal of Alloys and Compounds*, **2024**, 970, 172702.
[38] Otero A., SayaguéS M. a. J. S., Romero F. J., Gotor F. J., Moriche R. O. Piezoelectric and Dielectric Response of $BaTiO_3$/PVDF-TrFE Composites with High β‐Phase Content. *ACS Applied Polymer Materials*, **2025**, 7, 7848–7858.
[39] Im S., Cho S. Y., Cho J.-H., Hwang G.-T., Kingon A. I., Bu S. D., Jo W., Kim S.-H., Jeong C. K. Study on relaxor polymer interface matrix for piezoelectric nanocomposite generators. *Applied Surface Science*, **2023**, 613, 156031.
[40] Zhou S. Y., Zhang H. J., Du C. Z., Liu M., Liu L. M., Zhang Y. Chitosan-Doped PVDF Film with Enhanced Electroactive β Phase for Piezoelectric Sensing. *ACS Applied Electronic Materials*, **2024**, 6, 2575–2583.
[41] Sasmal A., Maity S., Maiti P., Arockiarajan A., Sen S. Nano to micrometer range particle size effect on the electrical and piezoelectric energy harvesting performances of hydroxide mediated crosslinked PVDF composites. *Chemical Engineering Journal*, **2023**, 468, 143794.
[42] Li Z. J., Wang X. Y., Jia M. G., Lu Y., Liu Y., Kang W. M. ZIF-67 Assists ultra-high piezoelectric output based on PVDF flexible nanogenerator. *Polymer*, **2024**, 312, 127623.
[43] Lu L. J., Ding W. Q., Liu J. Q., Yang B. Flexible PVDF based piezoelectric nanogenerators. *Nano Energy*, **2020**, 78, 105251.
[44] Tian G., Deng W. L., Gao Y. Y., Xiong D., Yan C., He X. B., Yang T., Jin L., Chu X., Zhang H. T., Yan W., Yang W. Q. Rich lamellar crystal baklava-structured PZT/PVDF piezoelectric sensor toward individual table tennis training. *Nano Energy*, **2019**, 59, 574–581.
[45] Chang S. M., Hur S., Park J., Lee D.-G., Shin J., Kim H. S., Song S. E., Baik J. M., Kim M., Song H.-C., Kang C.-Y. Optimization of piezoelectric polymer composites and 3D printing parameters for flexible tactile sensors. *Additive Manufacturing*, **2023**, 67, 103470.
[46] Ghosh M., Chakraborthy A., Castro V. O., Jin E., Heise K., Abuawwad L., Nuthalapati S., Senkovska I., Altinsoy M. E., Kaskel S., Nag A. MOF/PVDF Film for High-Performance Piezoelectric Haptic Devices. *ACS Applied Electronic Materials*, **2026**, 8, 3937–3950.
[47] Chen D. J., Sharma T., Zhang J. X. J. Mesoporous surface control of PVDF thin films for enhanced piezoelectric energy generation. *Sensors and Actuators A: Physical*, **2014**, 216, 196–201.
[48] Lee J.-H., Yoon H.-J., Kim T. Y., Gupta M. K., Lee J. H., Seung W., Ryu H. J., Kim S.-W. Micropatterned P(VDF-TrFE) Film-Based Piezoelectric Nanogenerators for Highly Sensitive Self-Powered Pressure Sensors. *Advanced Functional Materials*, **2015**, 25, 3203–3209.
[49] Yin F., Niu H., Kim E. S., Shin Y. K., Li Y., Kim N. Y. Advanced polymer materials‐based electronic skins for tactile and non‐contact sensing applications. *InfoMat*, **2023**, 5, e12424.
[50] Lv P. P., Zhan H., Zhang S. Z., Yang W. T., Xin L., Wang J., Li R. H., Li C. C., Ren L. C., Qian J., Zhang M. W. Vertically Aligned, Highly Ordered $BiFeO_3$‐$BaTiO_3$ Micropillars Supported by a Flexible P(VDF-TrFE) Layer for Harvesting Mechanical Energy and Sensing Applications. *ACS Applied Materials & Interfaces*, **2025**, 17, 61153–61163.
[51] Velic A., Hasan J., Li Z., Yarlagadda P. K. D. V. Mechanics of Bacterial Interaction and Death on Nanopatterned Surfaces. *Biophysical Journal*, **2021**, 120, 217–231.
[52] Peng R. B., Zhang B. T., Dong G. H., Wang Y. H., Yang G. N., Zhang J., Peng B., Zhao Y. N., Liu M. Enhanced Piezoelectric Energy Harvester by Employing Freestanding Single-Crystal $BaTiO_3$ Films in PVDF-TrFE Based Composites. *Advanced Functional Materials*, **2024**, 34, 2316519.
[53] Zhang X. H., Zhang C. G., Lin Y. H., Hu P. H., Shen Y., Wang K., Meng S., Chai Y., Dai X. H., Liu X., Liu Y., Mo X. J., Cao C., Li S. E., Deng X. L., Chen L. L. Nanocomposite Membranes Enhance Bone Regeneration Through Restoring Physiological Electric Microenvironment. *ACS Nano*, **2016**, 10, 7279–7286.
[54] IEEE Standard on Piezoelectricity. ANSI/IEEE Std 176-1987, 1988.
[55] Govindjee S. Stress. Engineering Mechanics of Deformable Solids: A Presentation with Exercises: Oxford University Press, 2012.
[56] Zhan H., Lv P., Zhang S., Xin L., Wang J., Li R., Li C., Ren L., Zhang M. High-performance piezoelectric composite combined with PZT micropillars and P(VDF-TrFE) membrane for energy harvesting and sensing. *Journal of Alloys and Compounds*, **2025**, 1019, 179227.
[57] Lv P., Zhan H., Zhang S., Yang W., Xin L., Wang J., Li R., Li C., Ren L., Qian J., Zhang M. Vertically Aligned, Highly Ordered $BiFeO_3$‐$BaTiO_3$ Micropillars Supported by a Flexible P(VDF-TrFE) Layer for Harvesting Mechanical Energy and Sensing Applications. *ACS Applied Materials & Interfaces*, **2025**, 17, 61153–61163.
[58] Zhao K., Shan Z., Li D., Ma R., Li P., Wang F., Cui Y., Zhong Z., Zhang K. PZT thick film element balancing flexibility with piezoelectricity fabricated by electrohydrodynamics jet printing used for micro power generator. *Ceramics International*, **2024**, 50, 26908–26917.
[59] Chamankar N., Khajavi R., Yousefi A. A., Rashidi A., Golestanifard F. A flexible piezoelectric pressure sensor based on PVDF nanocomposite fibers doped with PZT particles for energy harvesting applications. *Ceramics International*, **2020**, 46, 19669–19681.
[60] Yuan Y., Chen H., Xu H., Jin Y., Chen G., Zheng W., Wang W., Wang Y., Gao L. Highly sensitive and wearable bionic piezoelectric sensor for human respiratory monitoring. *Sensors and Actuators A: Physical*, **2022**, 345, 113818.
[61] Zhang Q., Li J., Li G., Du J., Xie C., Li H., Jin Y., He Y. Hierarchically structured hollow PVDF nanofibers for flexible piezoelectric sensor. *Chemical Engineering Journal*, **2024**, 498, 155661.
[62] Ham S. S., Lee G.-J., Hyeon D. Y., Kim Y.-G., Lim Y.-W., Lee M.-K., Park J.-J., Hwang G.-T., Yi S., Jeong C. K. Kinetic motion sensors based on flexible and lead-free hybrid piezoelectric composite energy harvesters with nanowires-embedded electrodes for detecting articular movements. *Composites Part B: Engineering*, **2021**, 212, 108705.
[63] Su Y., Chen C., Pan H., Yang Y., Chen G., Zhao X., Li W., Gong Q., Xie G., Zhou Y. Muscle fibers inspired high‐performance piezoelectric textiles for wearable physiological monitoring. *Advanced Functional Materials*, **2021**, 31, 2010962.
[64] Sharafkhani S., Kokabi M. Enhanced sensing performance of polyvinylidene fluoride nanofibers containing preferred oriented carbon nanotubes. *Advanced Composites and Hybrid Materials*, **2022**, 5, 3081–3093.
[65] Liu Z., Li G., Qin Q., Mi L., Li G., Zheng G., Liu C., Li Q., Liu X. Electrospun PVDF/PAN membrane for pressure sensor and sodium-ion battery separator. *Advanced Composites and Hybrid Materials*, **2021**, 4, 1215–1225.
[66] Wang S., Shao H.-Q., Liu Y., Tang C.-Y., Zhao X., Ke K., Bao R.-Y., Yang M.-B., Yang W. Boosting piezoelectric response of PVDF-TrFE via MXene for self-powered linear pressure sensor. *Composites Science and Technology*, **2021**, 202, 108600.
[67] Zhou X., Parida K., Halevi O., Liu Y., Xiong J., Magdassi S., Lee P. S. All 3D-printed stretchable piezoelectric nanogenerator with non-protruding kirigami structure. *Nano Energy*, **2020**, 72, 104676.

JET Accepted

[68] Mirjalali S., Bagherzadeh R., Abrishami S., Asadnia M., Huang S., Michael A., Peng S., Wang C. H., Wu S. Multilayered electrospun/electrosprayed polyvinylidene fluoride+ zinc oxide nanofiber mats with enhanced piezoelectricity. *Macromolecular Materials and Engineering*, **2023**, 308, 2300009.

[69] Singh H. H., Singh S., Khare N. Enhanced β - phase in PVDF polymer nanocomposite and its application for nanogenerator. *Polymers for Advanced Technologies*, **2018**, 29, 143–150.

[70] Oh S. R., Yao K., Chow C. L., Tay F. E. H. Residual stress in piezoelectric poly(vinylidene-fluoride-co-trifluoroethylene) thin films deposited on silicon substrates. *Thin Solid Films*, **2010**, 519, 1441–1444.

[71] Ye S. B., Cheng C., Chen X. M., Chen X. L., Shao J. Y., Zhang J., Hu H. W., Tian H. M., Li X. M., Ma L., Jia W. B. High-performance piezoelectric nanogenerator based on microstructured P(VDF-TrFE)/BNNTs composite for energy harvesting and radiation protection in space. *Nano Energy*, **2019**, 60, 701–714.

Just Accepted

Electronic Supplementary Material

Flexible pyramidal $BiFeO_3$–$BaTiO_3$ microcone arrays integrated with P(VDF-TrFE) for self-powered mechanical sensing and energy harvesting

Wentao Yang[1,§], Hang Zhan[1,§], Panpan Lv[1] ✉, Guiyun Gao[1], Shuzhi Zhang[1], Le Xin[2], Cuncheng Li[1], Luchao Ren[1], Jin Qian[3] ✉, and Mingwei Zhang[1,4,5] ✉

[1] *Discipline and Technology Center for High Temperature Functional Ceramics, Shandong Key Laboratory of Functional-Structural Integrated Ceramics, School of Materials Science and Engineering, Shandong University of Technology, Zibo 255000, China*
[2] *Department of Mathematics and Physics, Zibo Normal College, Zibo 255130, China*
[3] *Functional Materials Research Laboratory, School of Materials Science and Engineering, Tongji University, Shanghai 201804, China*
[4] *Analytical Testing Center, Shandong University of Technology, Zibo 255000, China*
[5] *Hubei Key Laboratory of Micro-Nanoelectronic Materials and Devices, Hubei University, Hubei 430062, China*
§ Wentao Yang and Hang Zhan contributed equally to this work.

✉ Address correspondence to Panpan Lv, lvpp@sdut.edu.cn; Jin Qian, j28_qian@163.com; Mingwei Zhang, zhang6666666@163.com

Supporting information to https://doi.org/10.26599/NR.2026.94909254

Supporting Note S1. Derivation of Stress Distribution in the Microcone Structure

The BFO-BTO microcone is approximated as an ideal truncated cone, and the axial coordinate z is defined from the cone tip ($z = 0$) to the cone base ($z = h$), where h is the microcone height and θ is the sidewall inclination angle. The local radius at position z can therefore be expressed as:

$$r(z) = r_{top} + z\ tan\theta \#(S1)$$

where r_{top} is the radius at the cone tip. Consequently, the local cross-sectional area is given by:

$$A(z) = \pi[r(z)]^2 = \pi(r_{top} + z\ tan\theta)^2 = A_{top}\left(1 + z\ \frac{tan\theta}{r_{top}}\right)^2 \#(S2)$$

where $A_{top}=\pi r_{top}^2$ is the tip cross-sectional area.

According to the force equilibrium condition, the axial stress distribution can be approximated as:

$$T(z) = \frac{F}{A(z)} \#(S3)$$

indicating that the stress decreases progressively from the cone tip toward the cone base due to the increasing cross-sectional area.

Just Accepted

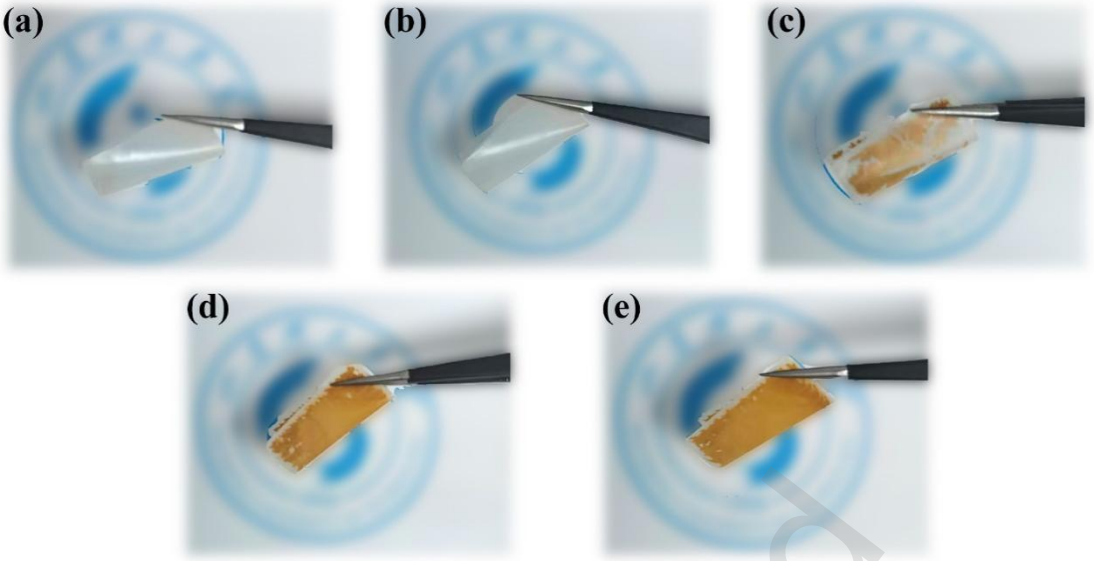


Fig. S1. Photographs of the BFO-BTO microcone/P(VDF-TrFE) composite films, where panels (a-e) correspond to microcone heights of 0.4, 0.9, 1.5, 2.5, and 3 μm, respectively.

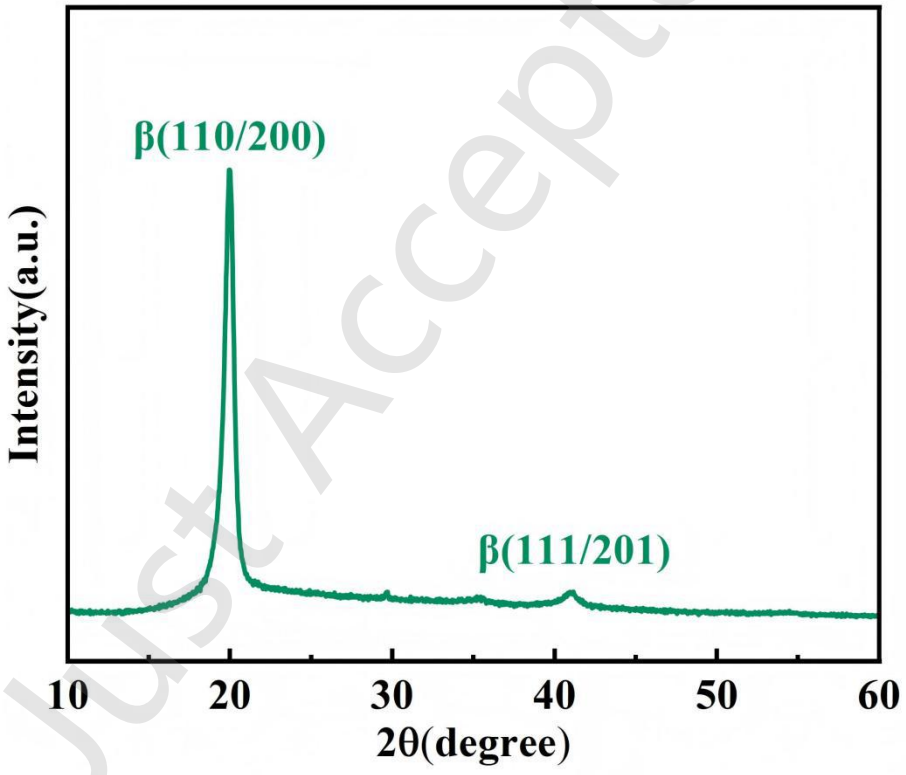


Fig. S2. X-ray diffraction (XRD) pattern of pure P(VDF-TrFE)

Just Accepted

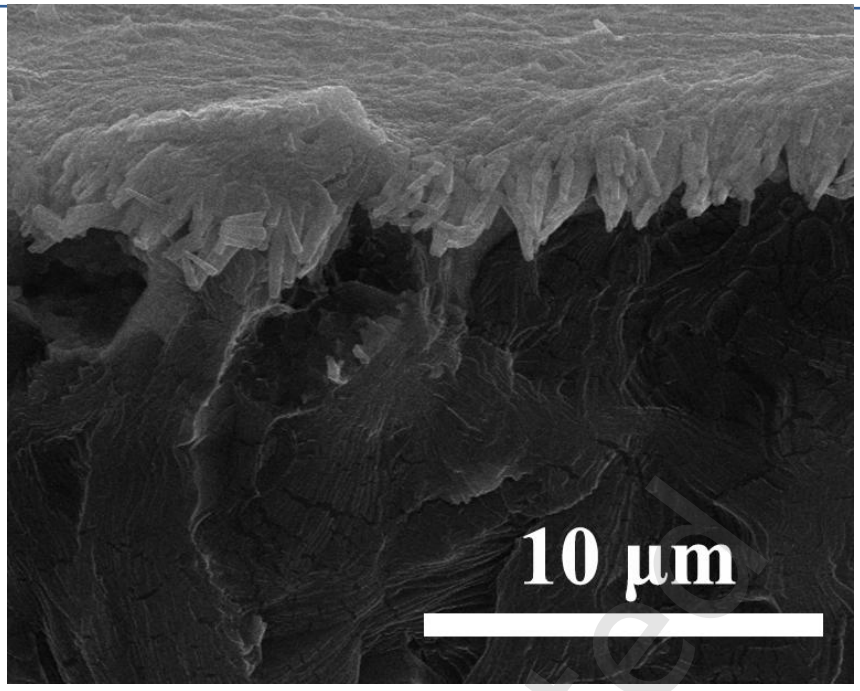


Fig. S3. Cross-sectional SEM image of the 3 μm BFO-BTO microcone/P(VDF-TrFE) composite film.

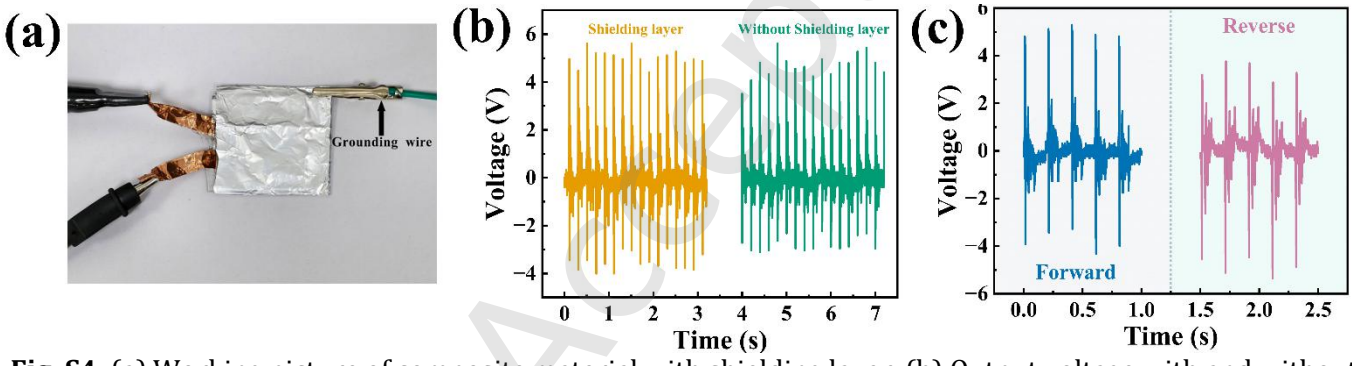


Fig. S4. (a) Working picture of composite material with shielding layer. (b) Output voltage with and without shielding layer. (c) V_{oc} achieved by the composite piezoelectric device with a conductive shielding layer in both forward and reverse connection modes.

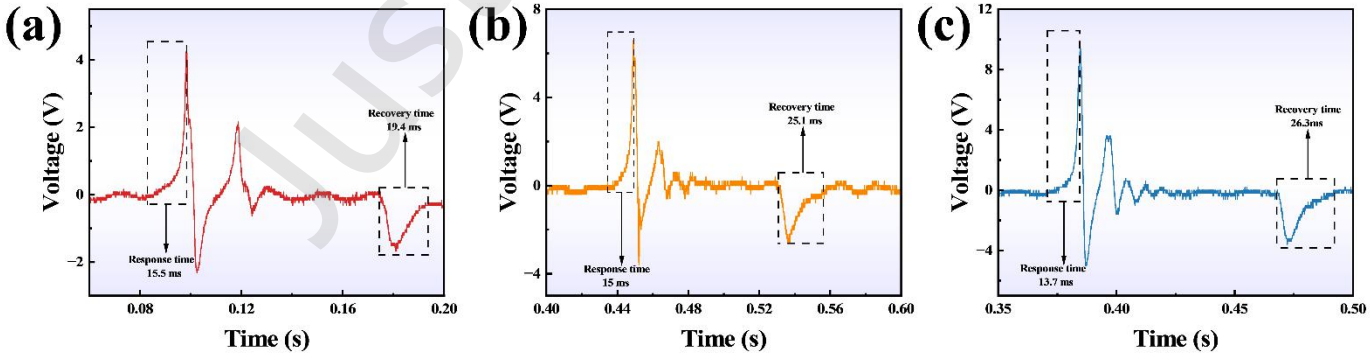


Fig. S5. (a-c) Dynamic response time of the 1.5 μm BFO-BTO/P(VDF-TrFE) composite piezoelectric device under applied forces of 0.6, 1, and 1.3 N, respectively.

Just Accepted

Table S1 Comparison of the piezoelectric and sensing performance of representative flexible piezoelectric composites.

Materials	Piezoelectric coefficient	Output performance	Sensitivity	Ref.
PVDF/ZnO nanoparticles	6.38 pC·N^{-1}	~3 V,254 nA	0.37 mV·kPa^{-1}	[1]
PVDF/ZnO nanorods	−1.17 pC·N^{-1}	1.81 V,0.57 mA	N/A	[2]
P(VDF-TrFE)/$BaTiO_3$ nanoparticles	20 pC·N^{-1}	6 V,2 mA·cm^{-2}	N/A	[3]
MXene/P(VDF-TrFE)	N/A	1.58 V	2.51 mV/ (μm N)	[4]
PAN/PVDF	N/A	1.3 V	1.3 V·N^{-1}	[5]
PVDF/CNTs	N/A	~6.8 V	1.28 V·N^{-1}	[6]
PVDF/PDA-$BaTiO_3$ nanoparticles	22.56 pC·N^{-1}	~14 V, ~0.53 mA	3.95 V·N^{-1}	[7]
P(VDF-TrFE)/KNN	72.62 pm·V^{-1}	~5 V, ~1 mA	N/A	[8]
PVDF nanofiber	N/A	10.1 V	2.7 V·N^{-1}	[9]
PVDF	N/A	0.24 V	0.24 V·N^{-1}	[10]
PZT/PVDF	N/A	0.184 V	0.08658 V·N^{-1}	[11]
PZT thick film	N/A	1.83 V	2.56 V·N^{-1}	[12]
PZT micropillar/P(VDF-TrFE)	N/A	7.36 V	3.52 V·N^{-1}	[13]
BFO-BTO micropillar /P(VDF-TrFE)	24 pC·N^{-1}	3.54 V	4.69 V·N^{-1}	[14]
BFO-BTO microcone /P(VDF-TrFE)	19 pC·N^{-1}	5.12 V	6.28 V·N^{-1}	This work

Description of the supporting videos.

Video S1. The process of lighting up a blue commercial LED lamp through continuous mechanical tapping of the sensor.

Video S2. The process of charging the capacitor through the rectified output under continuous mechanical tapping and subsequently discharging it to power the digital watch for an extended period.

References

[1] Mirjalali S., Bagherzadeh R., Abrishami S., Asadnia M., Huang S., Michael A., Peng S., Wang C. H., Wu S. Multilayered electrospun/electrosprayed polyvinylidene fluoride+ zinc oxide nanofiber mats with enhanced piezoelectricity. *Macromolecular Materials and Engineering*, **2023**, 308, 2300009.

[2] Singh H. H., Singh S., Khare N. Enhanced β‐phase in PVDF polymer nanocomposite and its application for nanogenerator. *Polymers for Advanced Technologies*, **2018**, 29, 143–150.

[3] Zhou X., Parida K., Halevi O., Liu Y., Xiong J., Magdassi S., Lee P. S. All 3D-printed stretchable piezoelectric nanogenerator with non-protruding kirigami structure. *Nano Energy*, **2020**, 72, 104676.

[4] Wang S., Shao H.-Q., Liu Y., Tang C.-Y., Zhao X., Ke K., Bao R.-Y., Yang M.-B., Yang W. Boosting piezoelectric response of PVDF-TrFE via MXene for self-powered linear pressure sensor. *Composites Science and Technology*, **2021**, 202, 108600.

[5] Liu Z., Li G., Qin Q., Mi L., Li G., Zheng G., Liu C., Li Q., Liu X. Electrospun PVDF/PAN membrane for pressure sensor and sodium-ion battery separator. *Advanced Composites and Hybrid Materials*, **2021**, 4, 1215–1225.

[6] Sharafkhani S., Kokabi M. Enhanced sensing performance of polyvinylidene fluoride nanofibers containing preferred oriented carbon nanotubes. *Advanced Composites and Hybrid Materials*, **2022**, 5, 3081–3093.

[7] Su Y., Chen C., Pan H., Yang Y., Chen G., Zhao X., Li W., Gong Q., Xie G., Zhou Y. Muscle fibers inspired high‐performance piezoelectric textiles for wearable physiological monitoring. *Advanced Functional Materials*, **2021**, 31, 2010962.

[8] Ham S. S., Lee G.-J., Hyeon D. Y., Kim Y.-G., Lim Y.-W., Lee M.-K., Park J.-J., Hwang G.-T., Yi S., Jeong C. K. Kinetic motion sensors based on flexible and lead-free hybrid piezoelectric composite energy harvesters with nanowires-embedded electrodes for detecting articular movements. *Composites Part B: Engineering*, **2021**, 212, 108705.

[9] Zhang Q., Li J., Li G., Du J., Xie C., Li H., Jin Y., He Y. Hierarchically structured hollow PVDF nanofibers for flexible piezoelectric sensor. *Chemical Engineering Journal*, **2024**, 498, 155661.

[10] Yuan Y., Chen H., Xu H., Jin Y., Chen G., Zheng W., Wang W., Wang Y., Gao L. Highly sensitive and wearable bionic piezoelectric sensor for human respiratory monitoring. *Sensors and Actuators A: Physical*, **2022**, 345, 113818.

[11] Chamankar N., Khajavi R., Yousefi A. A., Rashidi A., Golestanifard F. A flexible piezoelectric pressure sensor based on PVDF nanocomposite fibers doped with PZT particles for energy harvesting applications. *Ceramics International*, **2020**, 46, 19669–19681.

[12] Zhao K., Shan Z., Li D., Ma R., Li P., Wang F., Cui Y., Zhong Z., Zhang K. PZT thick film element balancing flexibility with piezoelectricity fabricated by electrohydrodynamics jet printing used for micro power generator. *Ceramics International*, **2024**, 50, 26908–26917.

[13] Zhan H., Lv P., Zhang S., Xin L., Wang J., Li R., Li C., Ren L., Zhang M. High-performance piezoelectric composite combined with PZT micropillars and P(VDF-TrFE) membrane for energy harvesting and sensing. *Journal of Alloys and Compounds*, **2025**, 1019, 179227.

[14] Lv P., Zhan H., Zhang S., Yang W., Xin L., Wang J., Li R., Li C., Ren L., Qian J., Zhang M. Vertically Aligned, Highly Ordered $BiFeO_3$- $BaTiO_3$ Micropillars Supported by a Flexible P(VDF-TrFE) Layer for Harvesting Mechanical Energy and Sensing Applications. *ACS Applied Materials & Interfaces*, **2025**, 17, 61153–61163.

First Accepted

Address correspondence to Panpan Lv, lvpp@sdut.edu.cn; Jin Qian, j28_qian@163.com; Mingwei Zhang, zhang6666666@163.com